NTNU – Trondheim
Norwegian University of
Science and Technology

Oxygen and related defects in Czochralski silicon crowns

Soraia Sofia Pascoa

Master's Thesis
Submission date: August 2014
Supervisor: Marisa Di Sabatino, IMTE
Co-supervisor: Guilherme Gaspar, IMT

Norwegian University of Science and Technology
Department of Materials Science and Engineering

"The real voyage of discovery consists not in seeking new landscapes, but in having new eyes."
Marcel Proust

Abstract

For the purpose of this thesis work, four n-type CZ silicon ingots with different crown tapered angle and shouldering area were characterized in order to understand the oxygen behavior and related defects on ingot top cuts and its influence on material lifetime. A p-type CZ silicon ingot was also characterized in order to have a reference material for comparison. Differences in lifetime between the crowns were observed and a strong correlation between the crown tapered angle and oxygen concentration and distribution was established. The crown with the higher tapered angle has the highest lifetime. In contrast, the crown with the lower crown tapered angle has the lowest lifetime. The crystal body quality can be influenced by the top ingot quality in what concerns the interstitial oxygen concentration and distribution. Thus, analyzing the early body of each ingot, it might be possible to predict the crystal body quality.

Key-words: n-type CZ silicon, crown tapered angle, shouldering area, lifetime, interstitial oxygen.

Acknowledgements

This thesis work had important support and encouragement without which this project would not have become reality.

I would like to express my gratitude to Prof. Marisa Di Sabatino, my supervisor at NTNU, for giving me the opportunity to do my thesis work at a prestigious university and for her professional guidance and advice. I am also thankful for the chance to contribute with my work to the seminar organized by the Casting and Solidification Group and for the opportunity to travel around Norway.

I would also like to thank to Prof. João Serra for accepting to be my supervisor at FCUL and for his useful recommendations on this thesis work.

I am particularly grateful for the assistance given by Guilherme Gaspar, for his willingness to give his time so generously. His patient guidance, valuable suggestions and constructive criticism during the development of my thesis were of outmost importance. He is a great friend who opened to me a world of opportunities.

Support given by Prof. Miguel Brito was a great help when I was practicing my laboratory skills before going to NTNU. He was a great teacher and, most important of all, an advisor long before I start this experience abroad.

My gratitude is also extended to Teresa Di Giovanni for her enthusiastic encouragement and support during this experience abroad. This experience would not have been the same without her.

I also wish to thank Ken Vidar Falch for his motivation and understanding since the first moment that we met.

Finally, I want to thank my family and friends for their support and encouragement throughout this amazing experience that changed my life.

Table of contents

Abstract 2
Acknowledgments 3
List of Figures 6
List of tables 10
1. Introduction 12
2. Theory of Semiconductors 12
2.1. Energy bands 12
2.2. Dopants and Impurities 13
3. Generation and Recombination 14
3.1. Generation and recombination of charge carriers 14
3.2. Recombination mechanisms 14
3.2.1. Direct band-to-band radiative recombination 15
3.2.3. Shockley-Read-Hall recombination 15
3.2.4. Surface recombination 16
4. Single crystal growth 16
4.1. Czochralski silicon crystal growth 18
4.2. Impurities in CZ silicon 21
4.2.1. Oxygen 22
4.3. Defects in CZ silicon 26
4.3.1. Defect classification 26
4.3.2. Incorporation of intrinsic point defects 28
4.3.2.1. Voronkov's Theory 28
4.3.2.2. Abe's Theory 29
4.3.3. Different grown-in microdefects 30
4.3.3.1. Interstitial-type defects (A/B defects) 30
4.3.3.2. Vacancy-type defects: voids (D-defects) 31
4.3.3.3. Vacancy-type defects: P-band, H-band and L-band 31
4.3.3.4. Perfect zone 32
4.3.3.5. Effect of impurities on microdefect formation 32
5. Characterization techniques 33
5.1. Preferential Etching 33
5.2. Lifetime Measurement Methods 34
5.2.1. Photoluminescence Imaging (PL) 34

5.3. Fourier-Transform Infrared Spectroscopy (FT-IR) 35
5.4. Four point probe (FPP) 36
5.5. Light microscope 37
6. Experimental details 38
6.1. Samples 38
6.2. Samples preparation 41
6.3. Oxygen and resistivity measurements procedure 42
6.4. Rapid Thermal Process (RTP) oven 43
6.5. Defect etching 44
6.6. Light microscope observations 44
6.7. Lifetime measurements 44
7. Results 45
7.1. Flow pattern defects (FPD) calculation method 45
7.2. Light microscope sensibility test 46
7.3. FPD density and P-band 47
7.4. Oxygen measurements in as-grown conditions 49
7.5. Thermal donors (TDs) dissolution 53
7.6. Comparison between n- and p-type materials 56
7.6.1. Oxygen and resistivity measurements in as-grown conditions 56
7.6.2. Thermal donors (TD) dissolution 59
8. Discussion 61
9. Conclusions 66
10. Further work 67
11. References 68

List of Figures

Figure 1 - Energy band diagrams for metal, semiconductor and an insulator [4] – this diagram illustrates a fundamental difference between insulating and conductive materials. 12
Figure 2 - Direct and Indirect band gap semiconductors, respectively [2,3]– (a) The conduction and valence band minimums are both located at the same wavenumber; (b) The conduction and valence band minimums are not both located at the same wavenumber. 13
Figure 3 - Defect levels of some elements in Silicon [5] – Ionization energies for some impurities in Silicon 14
Figure 4 – Schematic diagram of direct band-to-band radiative recombination [2] – direct electron-hole recombination assisted by a photon. 15
Figure 5 - Schematic diagram of Auger recombination [2] – three-particle interaction assisted by a phonon. 15
Figure 6 - Schematic diagram of Shockley-Read-Hall recombination [2] – recombination that involves trap states and is assisted by a phonon...16
Figure 7 – Surface recombination [9]: (a) silicon atoms are missing and unpaired valence alectrons exist forming electrically active interface traps, also called dangling bonds, (b) after oxidation most interface states are saturated with oxygen bonds, (c) after hydrogen passivation the surface amount of dangling bonds decreased...16
Figure 8 - Schematic representation of the Czochralski (CZ) and Float-zone (FZ) techniques, respectively [13] – single crystals can be grown by pulling them from the melt which was confined in a crucible or by a free-crucible technique which follows the vertical zone melting principle. 17
Figure 9 - Schematic of a typical CZ silicon growing system [16] – The grower system comprises the hot zone, crystal pull and rotation systems, crucible lift and rotation structures; diameter and temperature controlling devices...18
Figure 10 – Schematic of CZ crystal growth method [18] - The heating system is a meandering-coil element heated by electric current through a graphite element surrounding the silica crucible. The seed is lowered towards the melt and the necking process is performed. A dislocation-free crystal body grows...19
Figure 11 – Different steps of CZ crystal growth method [19] - The CZ crystal growth follows three major steps: (1) melting of polysilicon nuggets, (2) Temperature stabilization of the melt, (3) seeding processes, (4) necking process, (5) crown formation, (3) shouldering stage, (4) crystal body growth and (5) conic tail growth, which is not represented with a picture [16]. 19
Figure 12 - Convection patterns in a CZ melt due to (a) thermal convection, (b) crystal rotation and (c) crucible rotation [16] – Thermal convection flow due to the existence of a nonvertical temperature gradient and forced convection induced by crystal and crucible rotation. Seed rotation occurs in clockwise direction to homogenize impurities distribution and suppress temperature inhomogeneities; crucible rotation in counter-clockwise direction in order to stabilize the melt flow and control the oxygen concentration in the crystal. 21
Figure 13 - Typical heat flow pattern during the crystal pulling [22] - Silicon solidification is accompanied by latent heat generation. It is dissipated into the crystal via conduction which in turn dissipates heat to the ambient through radiation and convection 21
Figure 14 - Limits on impurity concentration in p-type silicon for impurities determining the degradation threshold of solar cells for (a) semiconductor, (b) solar-, and (c) MG-Si [23]. 22
Figure 15 - Schematic of a silicon CZ growth system showing relationship among oxygen-controlling factors – oxygen incorporation in the melt due to dissolution of crucible silica walls. Most of oxygen evaporates from the melt surface, but oxygen segregation into the crystal also occurs [25, 26]. 22

Figure 16 - Oxygen concentration measured as a function of the fraction of melt surface being covered by the growing crystal during crown growth [27] - relationship between oxygen concentration and available melt surface is not linear. The oxygen evaporation is very sensitive to the diameter change and the oxygen incorporation into the crystal will be related to that. 23
Figure 17 – Radial oxygen profile from the seed to the tail of the 300mm diameter crystal [27] - when the crystal is covering almost completely the melt surface, the evaporation seems to remain nearly constant and the oxygen concentration in the crystal is linear along the fraction solidified.................24
Figure 18 - Schematic representation of oxygen distribution in silicon melt at high and low melt level configurations [29] - The dots and lines represent oxygen concentration. (a) At atmospheric pressure, the oxygen distribution is not uniform near the melt centre, instead there is a low oxygen concentration region (b) At reduced pressure, the oxygen distribution appears to be more uniform near the melt surface and with superior radial oxygen uniformity [29]...24
Figure 19 –Maximum oxygen-related donor generation per hour of heat treatment at given temperatures [39] – The higher peak occur at around 450ºC and corresponds to thermal donors (TDs) generation; the lower peak occur at around 750ºC and it is due to new donors (NDs) formation.........26
Figure 20 - Overview of crystal defects in silicon lattice [41] – a – interstitial impurity atom, b – edge dislocation, c – self-interstitial atom, d – vacancy, e – precipitate of impurity atoms, f – vacancy-type dislocation loop, g – interstitial type dislocation loop, h – substitutional impurity atom......................28
Figure 21- Illustration of the dependence of defect pattern on V/G ratio [48] - When *V/G* is below the critical value, self-interstitials will dominate in the crystal. For *V/G* above the critical value, vacancies are incorporated...29
Figure 22 - Abe's proposal model on incorporation on grown-in defects in CZ crystal. Higher thermal gradient G>25ºC cm-1 (a) and lower G<20ºC (b) [49] - the defect incorporation is believed to be only dependent on thermal gradient *G* near the interface during growth rather on *V/G* ratio. 30
Figure 23 - Schematic spatial distribution of grown-in microdefect in an axial cross section near the critical V/G ratio and a mixed-type defects radial cross section, respectively [45, 51] - the defect-type will change from interstitial-type (A/B-defects) to vacancy-type (D-defects) in respect to *V/G* ratio and a defect-free gap is formed between the two regions. There are three distinct grown-in defect bands at the periphery of the vacancy defect region, namely P-band, H-band and L-band................................30
Figure 24 - A series of optical micrographs showing a flow pattern defect during a sucessive secco etching for (a) 1, (b) 14 and (c) 70 min. The amount of silicon removed is illustrated in the upper corner of each picture [59] – A FDP is shown in picture (a) but no etch pit can be seen at the nuclei site (D). In picture (b) is possible to see the void as a small etch pit. In picture (c), one more FPD is formed and some secco-etched pits (or shallow pits) are also delineated. 31
Figure 25 - Illustration of the processes of preferential etching and polishing etching, respectivley [72] – preferential etching delineates microdefects while polishing etching removes damage layers and smooth surfaces...33
Figure 26 - Typical illustration of an experimental setup for photoconductance-calibrated photoluminescence lifetime imaging - the entire sample area is excited by optical excitation. The resulting variation in PL-emission is measured with a CCD-camera resulting in a final image [82]....35
Figure 27 - Shematic of sample analysis process by FTIR [85] - the infrared light is collimated and directed to a beam splitter. The light is refracted towards towards the fixed mirror and transmitted to the moving mirror. All frequencies are being measured simultaneously and the interference between the lights reflected from both mirrors generates an interferogram. This signal is then transmitted to the detector which encodes the wavelength. The quantification of bond concentration is performed using Fourier transformation...36
Figure 28 - Schematic of four point probe [86] – there is two electrodes which supply current and other two which measure voltage. 36

Figure 29 - Simplified schematic drawing of the optical path of a ligh microscope in reflection mode [87] - the sample surface is illuminated and a magnified picture is produced by the reflected light through the use of lenses. 37
Figure 30 – Flow chart of measurements performed in this thesis....38
Figure 31 - Sample diameter as a function of length for all samples investigated. 39
Figure 32 – Lifetime (µs) measurements with PL imaging of the sample (a) C1N, (b) C2N, (c) C5N and (d) C6N under as-grown conditions - The crown with the higher tapered angle (C5N) has also the higher lifetime. In contrast, the crown with the lower crown tapered angle (C2N) has the lower lifetime. 40
Figure 33 - Samples area and average lifetime as a function of the growing time (crown and shoulder). 40
Figure 34 - Normalized average crown lifetime as a function of crown tapered angle – the relationship between lifetime and crown tapered angle is almost exponential. 41
Figure 35 - Schematic view of the samples preparation steps....41
Figure 36 - Cleaning process steps and following sample chemical polishing. 42
Figure 37 - Illustration about oxygen and resistivity measurements procedure - Six vertical lines followed. For each line, the measurements were carried out with 2mm of resolution. 43
Figure 38 – Light microscope images (a) The FPD density calculation method with 50x magnification and (b) Ilustration of D-defect , FDP and shallow pits (SP) with 100x magnification. 45
Figure 39 – FPD distribution for Line 1 of sample C5N following two different resolutions....46
Figure 40 – FPD distribution for Line 1 of sample C6N following two different resolutions....46
Figure 41 – Example of the possible FPD counting repetition due to manual sample movement. 47
Figure 42 - FPD density along the first line measured (ingot center) as a function of sample length of samples C2N and C5N, with 2 mm of resolution. The respective P-band position is also represented.47
Figure 43 - FPD density along the first line measured (ingot center) as a function of sample length of samples C1N and C6N, with 2 mm of resolution. The respective P-band position is also represented.48
Figure 44 - Light microscope pictures before transition for (a) C1N, (b) C2N, (c) C5N and (d) C6N.48
Figure 45 - Light microscope pictures after transition for (a) C1N with 733 FPD/cm^2 , (b) C2N with 557 FDPs/cm^2 , (c) C5N with 704 FPD/cm^2 and (d) C6N with 733 FPD/cm^2. 49
Figure 46 - Interstitial oxygen measurements along six vertical lines as a function of the sample length for (a) C1N, (b) C2N, (c), C5N and (d) C6N in as-grown conditions. 50
Figure 47 – Interstitial oxygen measurements along the first vertical line (ingot center) as a function of the sample length, for all samples in as-grown conditions 51
Figure 48 - Interstitial oxygen measurements along the first line (ingot center) of the early body as a function of the sample length, for all samples in as-grownconditons. 51
Figure 49 - Interstitial oxygen and resistivity measurements as a function of the sample radius for C2N in as-grown conditions. 52
Figure 50 - Interstitial oxygen and resistivity measurements as a function of the sample radius for C5N in as-grown conditions. 52
Figure 51 - Interstitial oxygen measurements along the first vertical line (ingot center) as a function of the sample length, for all samples after TDs annihilation. 53
Figure 52 - Interstitial oxygen measurements along the first line (ingot center) of the early body as a function of the sample length, for all samples after TD annealing. 53
Figure 53 - Resistivity measurements along the first vertical line (ingot center) as a function of the sample length, for all samples before TDs annihilation. 54
Figure 54 - Resistivity measurements along the first vertical line (ingot center) as a function of the sample length, for all samples after TDs annihilation. 54
Figure 55 – Resistivity difference between before and after TDs annihilation for all samples along the first vertical line (ingot center) as a function of the sample length. 55

Figure 56 - Average difference in resistivity between before and after TDs annihilation for the whole samples area. 55
Figure 57 - Lifetime (μs) measurements with PL imaging of the sample (a) C2N and (b) C5N, after TD annealing. 55
Figure 58 - Sample radius as a function of length for C2N and C2P. 56
Figure 59 - FPD density along the first line measured (ingot center) as a function of sample length of samples C2P and C2N, with 2 mm of resolution. The respective P-band position is also represented. 57
Figure 60 - FPD density along the third line measured as a function of sample length of samples C2P and C2N, with 2 mm of resolution. 57
Figure 61 - FPD density along the fifth line measured as a function of sample length of samples C2P and C2N, with 2 mm of resolution. 57
Figure 62 - Interstitial oxygen measurements along the first line (ingot center) for both samples C2N and C2P., before TDs annihilation. 58
Figure 63 - Resistivity and interstitial oxygen measurements along the first line (ingot center) for sample C2N, before TDs annihilation. 58
Figure 64 - Resistivity and interstitial oxygen measurements along the first line (ingot center) for sample C2P, before TDs annihilation. 58
Figure 65 - Resistivity and interstitial oxygen measurements along the first line (ingot center) for sample C2N, after TDs annihilation. 59
Figure 66 - Resistivity and interstitial oxygen measurements along the first line (ingot center) for sample C2P, after TDs annihilation. 59
Figure 67 - Dopant concentration for the average resistivity for the whole samples area, after TDs annihilation..60

List of tables

Table 1 - Typical range of concentration of impurities in semiconductor-grade CZ silicon crystals growth with or without a magnetic field [24]. 23
Table 2 - Classification of crystal defects in silicon [10, 34]. 27
Table 3 - Transition area (or shoulder area) and correspondent growing time for all samples under investigation. 39
Table 4 - Crown tapered angle and correspondent growing time for all samples under investigation .39
Table 5 - RTP oven cleaning steps 43
Table 6 - Thermal donor annihilation steps using a RTP oven 44

1. Introduction

"*... in 100 years people will say: the work is done, we are living in the Solar Age*."
Hermann Scheer, winner of the Right Livelihood Award
(The 'Alternative Nobel Prize')

In a world which also needs to meet the increasing energy demand, solar energy is definitely a good alternative. The PV industry keeps lowering the production costs and, consequently, the prices of solar systems. However, the silicon material quality and subsequent efficiency are still important issues. There are many impurities with great influence in the silicon performance and efforts are being directed at this subject. Among these impurities, oxygen stands out for its detrimental effects on solar cells performance.
The motivation of this thesis is to proceed with silicon material characterization in order to understand the oxygen behavior and related defects on ingot top cuts and its influence on material lifetime.

2. Theory of Semiconductors

A great concern in the industry is about the solar cell efficiency which depends substantially on the material quality. The most important microscopic parameter to characterize material quality is the carrier recombination lifetime, which will be explained later after briefly introducing semiconductors theory [1].

2.1. Energy bands

The simplified energy band diagram for semiconductors consists on two distinct bands: conduction band and valence band. In Figure 1, it is possible to identify both energy bands for metal, semiconductor and insulator situations. In the first case, an electron can move to the conduction band freely because there is no forbidden region (band gap) present. On the other hand, insulators have a band sufficiently large that electrons cannot make the transition to the conduction band. Finally, semiconductors fall somewhere in the between.
Generally, the bottom line which indicates the bottom edge of the conduction and is labeled E_c and the top of the valence band is indicated as E_v. The energy difference between those two bands is the energy band gap, namelly E_g or E_{gap} [2,3].

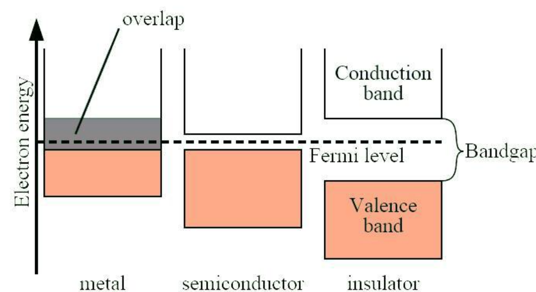

Figure 1 - Energy band diagrams for metal, semiconductor and an insulator [4] – this diagram illustrates a fundamental difference between insulating and conductive materials.

An important feature of an energy band diagram, which is not included on the simplified diagram, is whether or not the conduction band minimum and the valence band maximum occurs at the same value for the wavenumber (k). A semiconductor which minimum and maximum occurs for the same

wavenumber is called a direct band gap semiconductor. Otherwise, the semiconductor is said to have an indirect band gap. The nature of the band gap is important because of the way it affects the absorption and emission of light (see Figure 2). In terms of the $E - k$ diagrams (band diagrams) the energy is plotted as a function of the wavenumber (k) along the main crystallographic directions in the crystal, since the band diagram depends on the direction in the crystal. In case of direct band gap semiconductors like GaAs, the conduction and valence band minimums are both located at $k = 0$, while in indirect band gap semiconductors such as Si and Ge, they are located at different values of k. Since photons have relatively low momentum, a photon emission or absorption by a carrier can be thought of as making vertical transitions in the $\mathrm{E} - \mathrm{k}$ diagram. This means that, in a direct band gap semiconductor, carriers can relatively easily recombine via photon emission. In an indirect band gap semiconductor, electrons and holes are concentrated around different wave numbers, which means that recombination must involve, in addition to the photon, another particle for momentum to be conserved. Usually this assisting particle is a phonon [2,3].

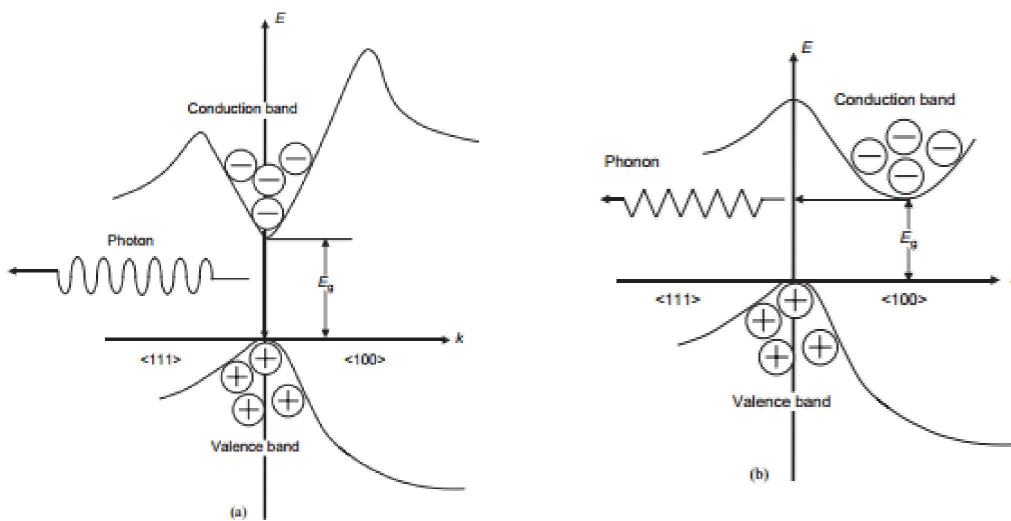

Figure 2 - Direct and Indirect band gap semiconductors, respectively [2,3]– (a) The conduction and valence band minimums are both located at the same wavenumber; (b) The conduction and valence band minimums are not both located at the same wavenumber.

2.2. Dopants and Impurities

Up until now, we were just discussing about intrinsic semiconductors, i.e., semiconductors which do not contain impurities. However, extrinsic semiconductors are of more interest for solar technology. In such semiconductors devices, a considerably higher number of charge carriers introduced by doping are present and the semiconductor is defined as extrinsic.

These impurities can be introduced unintentionally during the crystal growth or they can be added intentionally to increase the number of free carriers in the semiconductor [1].

When a controlled quantity of specific impurities is introduced in the intrinsic material, a doped material is obtained. However, generation of free carriers requires not only the presence of impurities, but also that those are able to give off electrons to the conduction band.
For instance, silicon is a group IV element in the periodic table, so for an n-type doping an element from group V (i.e. As, P) is chosen, as well for a p-type doping an element from group III is selected (i.e. B, Al, Ga, In). If the introduced impurity provides extra electrons to the conduction band, they are called donors. If the introduced impurity gives off holes to the valence band, they are called acceptors. In other words, if impurities are ionized, i.e., the impurity atoms either have donated or accepted an electron, the semiconductor material will consequently contain free carriers.

The ionization of the impurities is dependent on the thermal energy and the position of the impurity level within the energy band gap. In silicon we can have either shallow or deeper impurities. In the first case, defect levels are very near band gap edges and little energy is required to ionize. On the contrary, deeper defect levels (or traps) are located near the middle of band gap and more energy is needed to ionize the atoms. The latter can be effective recombination centers because of the high probability of electron-hole pairs annihilation. Ionization energies of some elements in silicon are shown in Figure 3 [1,3,5].

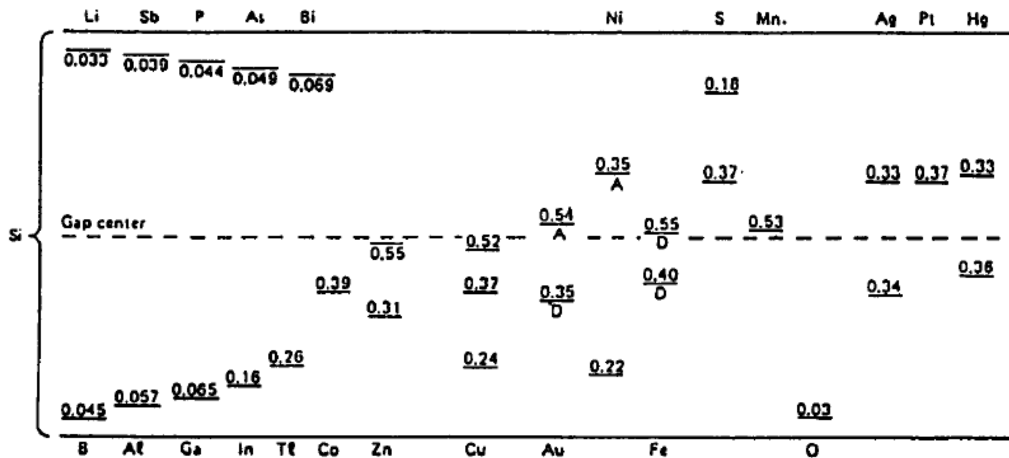

Figure 3 - Defect levels of some elements in Silicon [5] – Ionization energies for some impurities in Silicon

3. Generation and Recombination

3.1. Generation and recombination of charge carriers

The generation process consists of electron-hole pairs formation while the recombination process consists of its annihilation. When a semiconductor is exposed to light, excess carriers will be injected and then recombine with the carriers already present in the semiconductor returning to the equilibrium state. Thus, recombination lifetime (τ_R) is defined as the measure of the period of recovery of carriers from the perturbed state to the equilibrium. As well, carrier lifetime is defined as the time in which the excess carrier concentration has decreased to 1/e or 37% of this value in the steady state [2].

3.2. Recombination mechanisms

The most important recombination mechanisms will be discussed in this section and they are divided in intrinsic recombination and extrinsic recombination mechanisms. The first one consists of radiative band-to-band recombination (τ_{rad}) and Auger recombination (τ_{Auger}). The second is an indirect phonon-assisted recombination which is known as Shockley-Read-Hall (SRH) recombination (τ_{SHR}). Equation 1 represents both material surface and bulk lifetimes (τ_{sup} and τ_{bulk}, respectively) contribution to the effective lifetime ($\tau_{effective}$) [6].

$$\frac{1}{\tau_{effective}} = \frac{1}{\tau_{bulk}} + \frac{1}{\tau_{sup}} = \left(\frac{1}{\tau_{rad}} + \frac{1}{\tau_{SHR}} + \frac{1}{\tau_{Auger}}\right) + \frac{1}{\tau_{sup}} \tag{1}$$

3.2.1. Direct band-to-band radiative recombination

In direct band-to-band radiative recombination, an electron from conduction band descends to the valence band where recombines directly with a hole and consequently energy dissipation in the form of photon (Figure 4) [6].

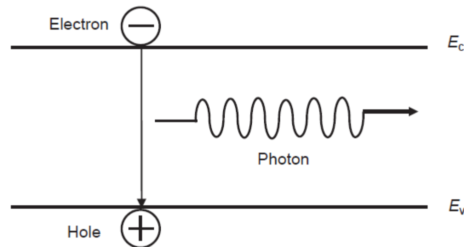

Figure 4 – Schematic diagram of direct band-to-band radiative recombination [2] – direct electron-hole recombination assisted by a photon.

3.2.2. Auger recombination

Auger recombination is a three-particle interaction where two similar carriers collide, either the electron-electron collision in the conduction band followed by recombination with a hole in the valence band, or hole-hole collision in the valence band followed by recombination with an electron in the conduction band. The excited carrier eventually releases its excess energy as a phonon to the crystal [6]. A schematic diagram of Auger recombination is presented in Figure 5.

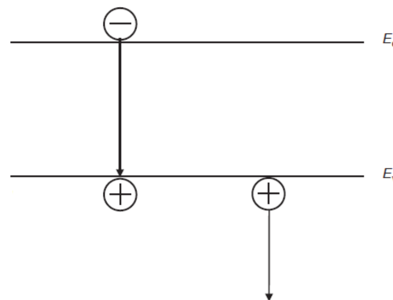

Figure 5 - Schematic diagram of Auger recombination [2] – three-particle interaction assisted by a phonon.

The recombination occur in a band-to-band transition, thus the expression for the net recombination rate is similar to that of band-to-band recombination [7,8].

3.2.3. Shockley-Read-Hall recombination

Shockley-Real-Hall recombination (SRH) is an indirect recombination mechanism that involves defect or trap states which serve mainly to capture and release carriers (Figure 6). These trap states are energy levels created due to the presence of impurities or crystallographic imperfections within the semiconductor. When these trap states capture both types of carriers they are called recombination centers and these are usually located around and in the mid gap [6].

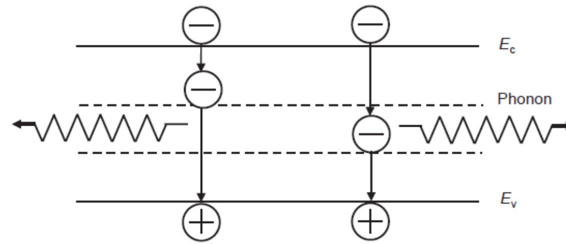

Figure 6 - Schematic diagram of Shockley-Read-Hall recombination [2] – recombination that involves trap states and is assisted by a phonon.

There are four possible interaction mechanisms of free carriers with a defect level in the band gap. The defect level can be occupied either by an electron (occupied state) or by a hole (unoccupied state). On one hand, occupied states can either emit its electron into the conduction band or capture a hole from the valence band. On other hand, unoccupied states can either capture an electron from the conduction band or emit its hole into the valence band.

From the four emission and capture processes, it is possible to deduce rate equations which describe the SRH model. For this purpose, it is assumed that the semiconductor is nondegenerate and that the density of trap states is small compared to the majority carrier density.

3.2.4. Surface recombination

Recombination at surfaces is often enhanced relative to the bulk due to the presence of surface dangling bonds which act as trapping centers [2]. The surface recombination can be reduced by surface passivation. Passivation is done in several different ways. One way is to use an appropriate dielectric surface layer such as a silicon oxide layer or a silicon nitride layer so that many of the dangling silicon bonds are passivated with oxygen or nitrogen and hydrogen atoms instead of acting as recombination centers (see Figure 7).

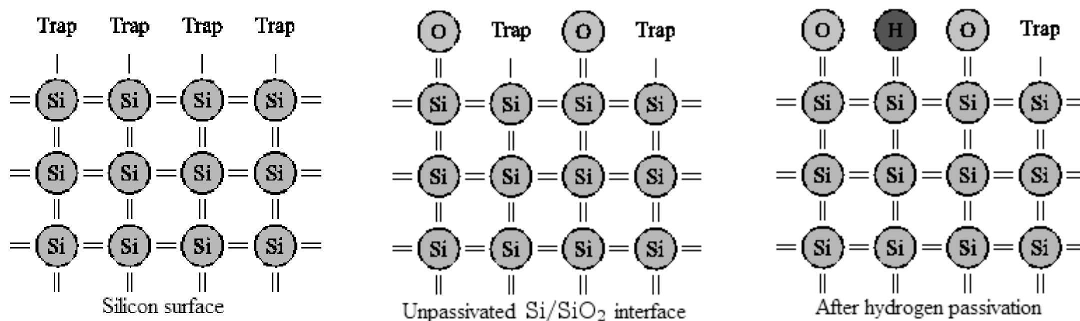

Figure 7 – Surface recombination [9]: (a) silicon atoms are missing and unpaired valence alectrons exist forming electrically active interface traps, also called dangling bonds, (b) after oxidation most interface states are saturated with oxygen bonds, (c) after hydrogen passivation the surface amount of dangling bonds is decreased**.**

4. Single crystal growth

Single crystals are grown either by the Czochralski (CZ) technique or the Float-Zone (FZ) technique, which are represented in Figure 8.

In 1916, Jan Czochralski (1885-1953), a polish metallurgist, developed a method for single crystal growth, later named the Czochralski method, as a result of an experimental accident. Czochralski

determined the crystallization rate of metals by pulling them out from the melt which was confined in a crucible [10]. Single crystals wires occurred and he recognized that single crystals could be grown using this technique. Nevertheless, the pulling technique was developed later by Teal and Little and patented in 1950 [11].

In CZ technique, a single crystal is grown by pulling upwards a monocrystalline seed with a given crystal orientation from the melt which is kept in a crucible. Through this method, it is possible to produce large and dislocation-free ingots. More about this crystal growth technique will be discussed in the next chapters.

In 1962, Henry C. Theuerer (1910-1988) patented a new method for single crystal growth, the FZ method [12].

This technique is based on vertical zone melting principle. Firstly, a monocrystalline silicon seed must be in contact with one end of a polycrystalline silicon ingot. Then a molten region is established by heating from a radio-frequency induction coil and starts to move vertically along the entire ingot and, simultaneously, purifying the material, forming dislocation-free monocrystalline silicon with the same crystallographic orientation of the starting seed.

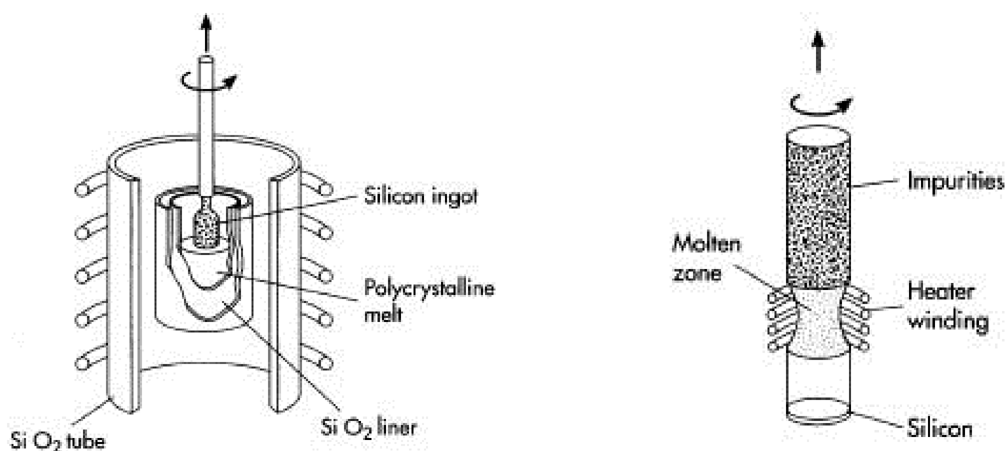

Figure 8 - Schematic representation of the Czochralski (CZ) and Float-zone (FZ) techniques, respectively [13] – single crystals can be grown by pulling them from the melt which was confined in a crucible or by a free-crucible technique which follows the vertical zone melting principle.

Both techniques have advantages which differ essentially in production cost and speed, which favor the CZ technique, and purity of the material, which is superior if the FZ method is carried out.

If the purity level is the main factor of interest, the FZ technique is the elected one mainly because it is crucible-free. Also, most of the impurities are more soluble in the molten silicon than in the crystal. Consequently, in FZ technique, those impurities are pushed away from the crystal. This procedure can be repeated more than one time in order to lower the remaining impurity concentration. This represents a huge advantage in relation to CZ technique, since it can achieve much higher purity and higher resistivity. On the other hand, a CZ crystal can have lower purity but it makes silicon wafers even more resistant against thermal stress and metallic contamination. Also, in the FZ technique, due to the molten region, the weight of the lower part of the crystal is quite restricted and only crystals with small diameter of up to 200 mm can be grown, while CZ crystals can be produced with diameters of up to 300 mm [14]. Therefore, if large crystal diameters and high doping concentration are required,

the CZ technique must be chosen, since it is difficult to be produced by FZ method. Besides the material quality, the production costs are also taken into account and CZ technique is the best option in concern to that matter. In fact, for the CZ technique, significant cost reductions can be accomplished by producing crystals with larger diameters and reusing the expensive crucibles.

Today, single crystals are produced mostly by the CZ technique, whereas the FZ technique is only essential for applications which require extremely pure silicon material.

During this chapter, the Czochralski technique will be discussed, in particular the silicon purification process, the CZ crystal growth and related impurities.

4.1. Czochralski silicon crystal growth

The Czochralski (CZ) method is used to convert polycrystalline silicon into single-crystal ingots of semiconductors [15]. This method requires rather complex equipment with several components and functions.

Figure 9 shows the typical CZ silicon growing system where the main components are exemplified. It is mainly composed by the so-called hot zone that includes the graphite susceptor, the graphite heater and the thermal shield; crystal pull and rotation systems, crucible lift and rotation structures; diameter and temperature controlling devices [16].

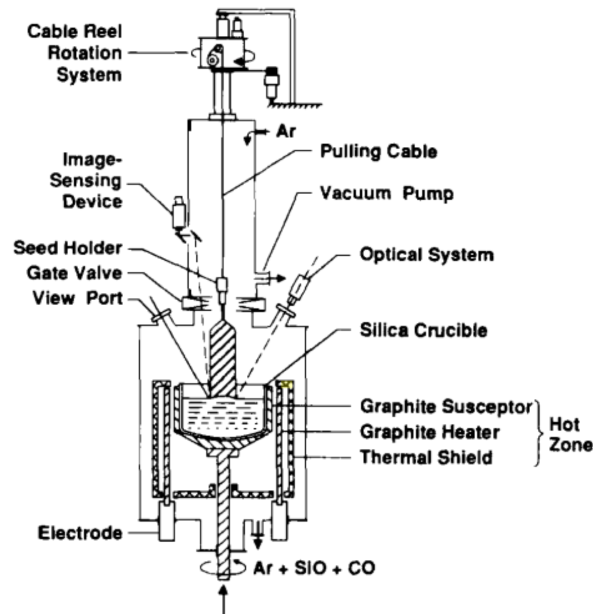

Figure 9 - Schematic of a typical CZ silicon growing system [16] – The grower system comprises the hot zone, crystal pull and rotation systems, crucible lift and rotation structures; diameter and temperature controlling devices.

The graphite hot zone is thermally insulated and it surrounds the silica crucible. The heating system is a meandering-coil element heated by electric current. A vacuum system is required, so at beginning of the crystal growth process the chambers are evacuated and then purged with inert gas, typically argon (Ar) at low pressure (5-50 mbar in PV industry and atmospheric pressure in microelectronic industry) [17].

The CZ crystal growth follows three major steps: (1) melting of polysilicon nuggets, (2) temperature stabilization of the melt, (3) seeding processes, (4) necking process, (5) crown formation, (3) shouldering stage, (4) crystal body growth and (5) conic tail growth [16].

Polysilicon nuggets are placed in a high-purity silica crucible which is heated to the melting point (1420ºC) [15, 16]. The seed holder is affixed to a steel cable or onto the upper shaft. Once the charge is molten, the melt flow needs to be stabilized under steady conditions before a rotational monocrystalline seed is lowered towards the melt which is rotating in the opposite direction of the seed. When dipped into the melt, the seed is pulled upward, melt crystallization begins at the solid-liquid interface and a monocrystalline silicon ingot grows with the desired diameter by adjusting the pull rate and melt temperature [15, 16]. Figures 11 and 12, show the CZ crystal growth process and the major steps, respectively.

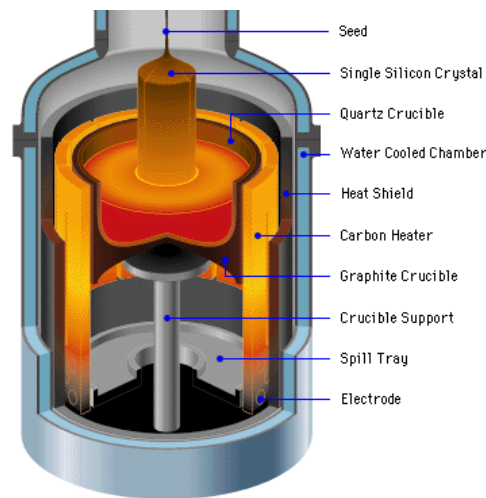

Figure 10 – Schematic of CZ crystal growth method [18] - The heating system is a meandering-coil element heated by electric current through a graphite element surrounding the silica crucible. The seed is lowered towards the melt and the necking process is performed. A dislocation-free crystal body grows.

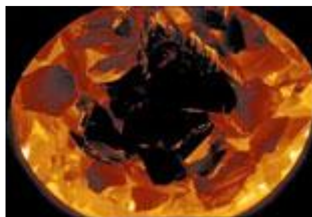
Melting of polysilicon nuggets

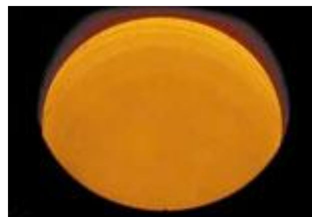
Temperature stabilization

Seeding process

Necking process

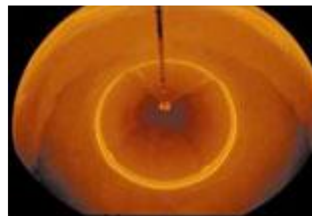
Shoulder growth

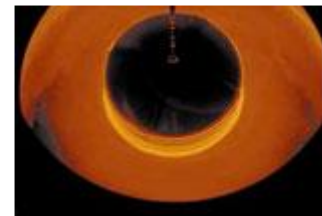
Crystal body growth

Figure 11 – Different steps of CZ crystal growth method [19] - The CZ crystal growth follows three major steps: (1) melting of polysilicon nuggets, (2) Temperature stabilization of the melt, (3) seeding processes, (4) necking process, (5) crown formation, (3) shouldering stage, (4) crystal body growth and (5) conic tail growth, which is not represented with a picture [16].

When the seed is dipped into the melt, dislocations in the material are generated due to a high thermal shock exposure. In order to achieve dislocation-free growth, “necking” process is performed. Since the ingot is typically pulled in a defined <100> orientation and dislocations only propagate on (111) planes that are oblique to that one, then dislocations grow out of the crystal neck after a few centimeters, thus the crystal body grows dislocation-free. Actually, this dislocation-free state manifests itself through the development of ridges on the crystal surface [17].

During the necking development, based on Dash (1958) [20], the seed with initial diameter of ~12mm is gradually decreased by increasing pull speed and temperature adjustment until both neck diameter of 3-4mm and a pull rate of 4-6mm/min are achieved, which happens after a few centimeters of growth [16].

After the necking process, the crystal diameter can be enlarged by slower pulling until it reaches the desired values the so-called “crown” formation. In the transition to the body growth status, the pulling velocity is raised to the specific value at which the crystal grows with the required diameter. This quick step is called the “shouldering stage”.

As long as the crystal body is growing, the pulling velocity is kept constant, in the range from 0.5 to 1.2 mm/min. Also, due to seed rotation the crystal cross-section is typically circular and the crystal diameter is often chosen between 150 and 200mm [17].

The contact at solid-liquid interface is established between the melt and the crystal. There the melt surface forms a meniscus to the crystal. This meniscus has the form of a shiny ring around the crystal and is the only option for crystal diameter control. This can be done through meniscus height variations control or by meniscus diameter measurement with a CCD camera. Therefore, the crystal diameter can be adjusted by controlling the pulling rate [17].

The melt is systematically stirred during the entire crystal growth process due to crystal seed and crucible rotation. The seed rotation occurs in clockwise direction to homogenize impurities distribution and suppress temperature inhomogeneities in the field. In the other hand, the crucible rotation in counter-clockwise direction in order to stabilize the melt flow and control the oxygen concentration in the crystal. Therefore, helical growth geometry is produced as result of those rotational movements and any small temperature variation inevitably would generate fluctuations in the growth rate. Defects formation can occur as a consequence [17, 21]. Figure 12 shows the convection patterns in a CZ melt.

Silicon solidification is accompanied by latent heat generation, which needs to be removed in order to not prevent further silicon solidification. Thus, it is dissipated into the crystal via conduction which in turn dissipates heat to the ambient through radiation and convection [21]. Figure 13 illustrates the typical heat flow pattern during the crystal pulling.

At the final stage of crystal growth, the crystal diameter decreases with the pull speed raising and crystal diameter decreasing. Gradually, it develops a “conic tail”. Afterward, the crystal can be separated from the melt free of dislocation formation in the crystal body [17].

After the crystal growth is finished, the heating system is turned off and the crystal remains in the grower for a period of time until it is approximately the room temperature before its removal from there. All temperature variations at which the crystal was subjected over time constitute the so-called thermal history of the silicon crystal, which is important to the material characterization [16].

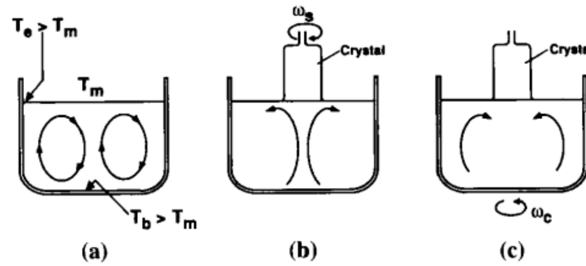

Figure 12 - Convection patterns in a CZ melt due to (a) thermal convection, (b) crystal rotation and (c) crucible rotation [16] – Thermal convection flow due to the existence of a nonvertical temperature gradient and forced convection induced by crystal and crucible rotation. Seed rotation occurs in clockwise direction to homogenize impurities distribution and suppress temperature inhomogeneities; crucible rotation in counter-clockwise direction in order to stabilize the melt flow and control the oxygen concentration in the crystal.

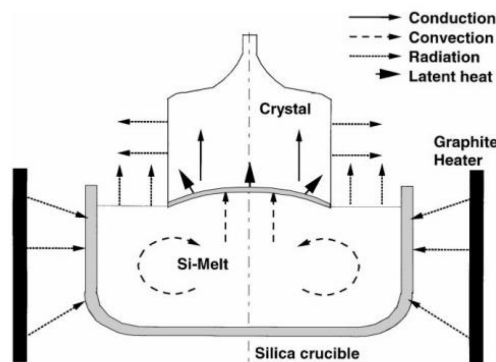

Figure 13 - Typical heat flow pattern during the crystal pulling [22] - Silicon solidification is accompanied by latent heat generation. It is dissipated into the crystal via conduction which in turn dissipates heat to the ambient through radiation and convection

4.2. Impurities in CZ silicon

It is known that certain impurities in as-grown silicon material will influence the solar cell performance. In Figure 14, the relationship between impurity type and material efficiency for p-type semiconductor is shown. The properties of the bulk material may be affected by electrically active impurity, increasing recombination rate. Furthermore, impurities may induce series- or shunt-resistance effects and other junction defect mechanisms. However, not all impurity and defect interaction phenomena are harmful to solar-cell performance. Oxygen precipitates can provide a significant benefit to CZ-Si, since those are able to trap unwanted metallic impurities. In Figure 15 it is shown the sensitivity of monocrystalline CZ solar cell performance in relation to different type and concentration of impurities.

Because the main focus of the thesis work is to investigate the role of oxygen and defects in CZ silicon materials, the following paragraph describes the current knowledge about oxygen in silicon and its effect on solar cell properties.

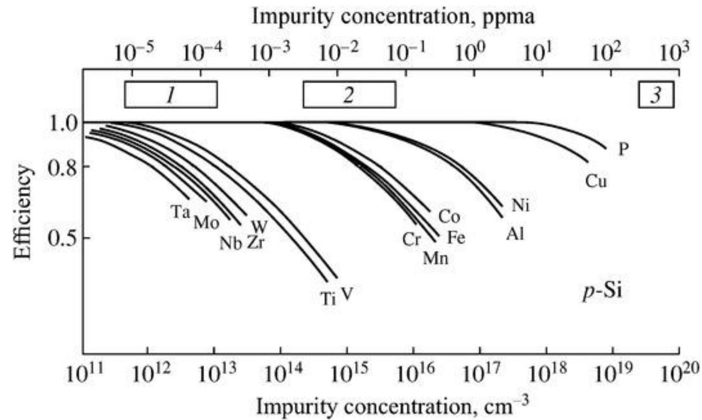

Figure 14 - Limits on impurity concentration in p-type silicon for impurities determining the degradation threshold of solar cells for (a) semiconductor, (b) solar-, and (c) MG-Si [23].

4.2.1. Oxygen

Oxygen is the most important unintentional impurity in CZ-Si, which is present in a range of 10^{18} atoms/cm^3 (see Table 1). The incorporation of this impurity in the melt results from the gradual dissolution of the silica crucible walls [24]. Equation 2 shows the respective reaction.

$$SiO_2 + Si \rightarrow 2SiO \quad (2)$$

Since SiO is very volatile, most of the oxygen evaporates from the melt surface, but a small part remains in the melt which is incorporated into the silicon crystal through the crystal-melt interface [25] (see Figure 15). The oxygen solubility depends on several factors such as the doping, the presence of carbon, thermal stress in the crystal, or even the ambient atmosphere during the process. Consequently, the oxygen content varies with the process growth conditions [26].

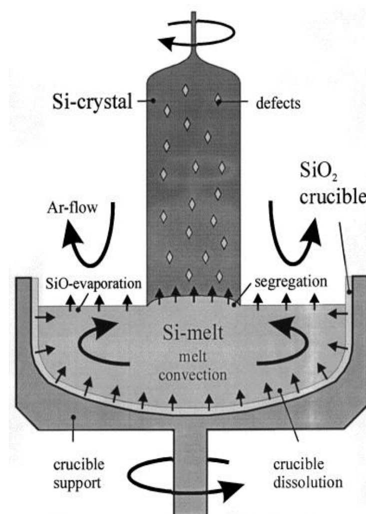

Figure 15 - Schematic of a silicon CZ growth system showing relationship among oxygen-controlling factors – oxygen incorporation in the melt due to dissolution of crucible silica walls. Most of oxygen evaporates from the melt surface, but oxygen segregation into the crystal also occurs [25, 26].

Therefore, the foremost oxygen-controlling factors in CZ-Si growth are the effect of surface evaporation and crucible dissolution. The effects of crystal and crucible rotations play also an important role in this matter [27].

Lin and Benson [27] studied the oxygen evaporation from the melt surface by growing a CZ crystal with 300 mm of diameter. During this experiment, the oxygen content was measured as a function of the fraction of melt surface being covered by the growing crystal during the growth process (see Figure 16). It was recognized that the relationship between oxygen concentration and available melt surface is not linear. Under a crystal diameter of 125 mm, the oxygen evaporation is very sensitive to the diameter change. Therefore, the oxygen concentration that still remains in the growing crystal will be related to that, following the diameter changing's. Though, when the crystal is covering almost completely the melt surface, i.e., when the crystal reaches the desirable diameter, the evaporation seems to remain nearly constant and the oxygen concentration in the crystal is linear along the fraction solidified. Figure 17 shows the radial oxygen profiles from the seed to the tail of the 300 mm diameter crystal. The maximum oxygen evaporation corresponds to 30% of the available dissolved oxygen. Still, much lower than generally conceived, that over 90% of the dissolved oxygen from crucible is evaporated from the melt surface [27].

Table 1 - Typical range of concentration of impurities in semiconductor-grade CZ silicon crystals growth with or without a magnetic field [28].

Impurity	Typical concentration	
Specified acceptor or donor dopant*	0.1 ppba… 1000 ppma	5×10^{12}… 5×10^{19} cm^{-3}
Other acceptors or donors	<1 ppba	$<5\times10^{13}$ cm^{-3}
Oxygen*	5-18 ppma	2.5×10^{17}… 9×10^{17} cm^{-3}
Carbon	<0.5 ppma	$<2.5\times10^{16}$ cm^{-3}
Iron	<1 ppta	$<5\times10^{10}$ cm^{-3}
The concentrations of the impurities denoted by the asterisk (*) are controlled to their optimized and/or specified values, while other impurities are considered to be contamination. Notice that 1 ppma corresponds to 5×10^{16} atoms/cm^3. The interstitial oxygen concentrations are given in "new ASTM units" (ASTM F 121-83) and carbon concentration are given in ASTM F 123-86 units.		

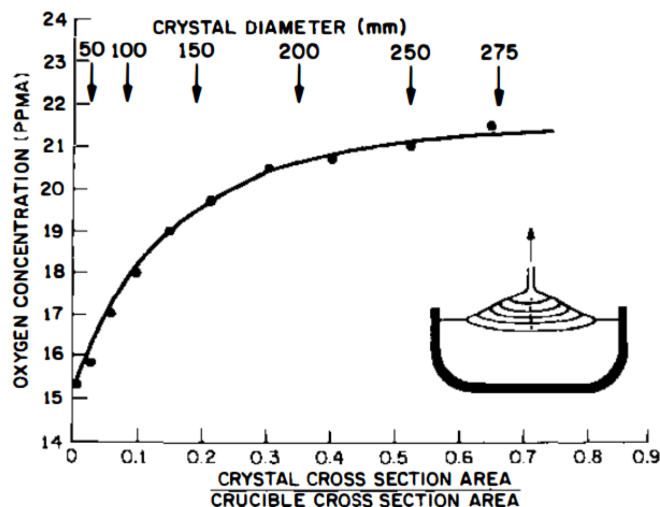

Figure 16 - Oxygen concentration measured as a function of the fraction of melt surface being covered by the growing crystal during crown growth [27] - relationship between oxygen concentration and available melt surface is not linear. The oxygen evaporation is very sensitive to the diameter change and the oxygen incorporation into the crystal will be related to that.

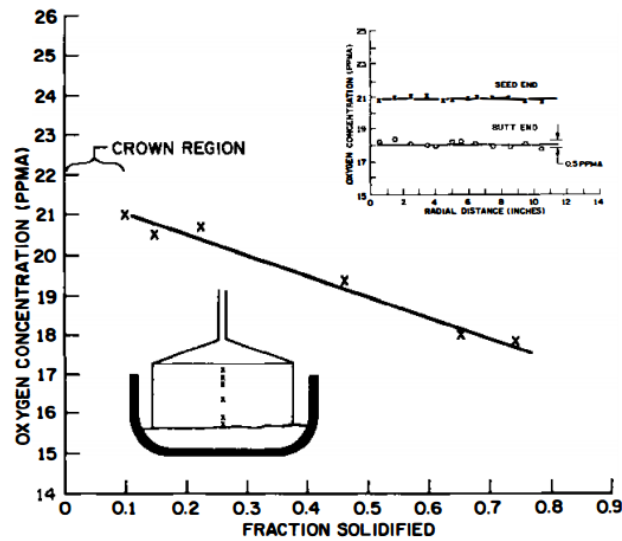

Figure 17 – Radial oxygen profile from the seed to the tail of the 300mm diameter crystal [27] - when the crystal is covering almost completely the melt surface, the evaporation seems to remain nearly constant and the oxygen concentration in the crystal is linear along the fraction solidified.

The effect of ambient pressure on the oxygen distribution in the melt and crystal was also studied by Lin and Benson [27]. In Figure 18 are represented the physical models of oxygen distributions in silicon melt which were proposed. It is illustrated that thermal convection is the main transport mechanism of this impurity. Is also clear that under atmospheric pressure (see Figure 18a) the oxygen distribution is not uniform near the melt centre, instead there is a low oxygen concentration region. This phenomenon is displayed in the radial oxygen profile of the crystal near the seed. However, as the crystal is keep growing, the forced convection achieved by crystal rotation modifies the oxygen distribution and, as a result, its non-uniformity in the melt is reduced. On the other hand, under reduce pressure (see Figure 18b) the oxygen distribution appears to be more uniform near the melt surface, thus with superior radial oxygen uniformity [27, 29].

Thermal convection is not significant in the case of a low ratio between melt-crucible contact and available free surface area. Then, the oxygen concentration in the melt is equally diffusion and crucible dissolution rate-dependent. The variation of this ratio is the basic characteristic of the axial oxygen profile of CZ silicon crystals and tends to decrease during its process growth. Consequently, the melt turns to be more uniform in oxygen content [27].

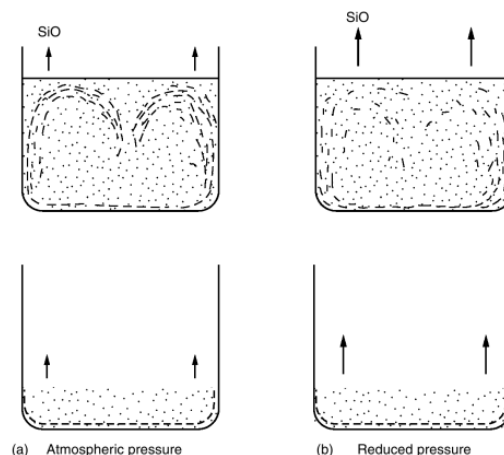

Figure 18 - Schematic representation of oxygen distribution in silicon melt at high and low melt level configurations [29] - The dots and lines represent oxygen concentration. (a) At atmospheric pressure, the oxygen distribution is not uniform

near the melt centre, instead there is a low oxygen concentration region (b) At reduced pressure, the oxygen distribution appears to be more uniform near the melt surface and with superior radial oxygen uniformity [29].

Once the oxygen is incorporated it can considerably affect the electrical, mechanical and physical crystal properties. In fact, oxygen precipitates provide a significant benefit to CZ-Si, since those are able to trap unwanted metallic impurities (Cu, Ni, Fe) [30], process known as *gettering* [31]. Actually the importance of the gettering process is very recognized by CZ-Si manufacturers. Therefore, they use a thermal treatment after wafer production to allow out-diffusion of oxygen which is near the wafer surface, forming a small oxygen-free layer in that region, the so-called *denuded-zone*, which improves the wafer performance.

When incorporated into the crystal, oxygen has an interstitial configuration and when dissolved it leads to an increase in the silicon lattice constant. However, interstitial oxygen is electrically inactive in the form that is incorporated. Though, depending on the thermal history during the crystal cooling, different stages of oxygen precipitation can be observed [26].

Upon temperatures around 450ºC, electrically active oxygen agglomerates are generated from the presence of interstitial oxygen [32]. These electrically active centres [33] are known as *thermal donors* (TDs) and their concentration has a linear relationship with interstitial oxygen concentration, being proportional to the fourth power of the latter [34]. Unlike standard doping impurities, TD introduces two different energy levels in the Si gap, located at 75 and 170 meV below the conduction band edge, respectively [35]. Therefore, TD are double donors in p-type Si whatever the hole concentration and in n-type Si up to an electron density of around $5\times10^{15}cm^{-3}$. All the silicon crystals experience this temperature range during the cooling process from the melt temperature to room temperature, when oxygen becomes supersaturated and may precipitate. Fortunately, TDs can be eliminated by a heat treatment around 800ºC [36].

Upon temperatures around 450ºC, electrically active oxygen agglomerates are generated from the presence of interstitial oxygen [32]. These electrically active centres [33] are known as *thermal donors* (TDs) and their concentration has a linear relationship with interstitial oxygen concentration, being proportional to the fourth power of the latter [34]. Unlike standard doping impurities, TD introduce two different energy levels in the Si gap, located at 75 and 170 meV below the conduction band edge, respectively [35]. Therefore, TD are double donors in p-type Si whatever the hole concentration and in n-type Si up to an electron density of around $5\times10^{15}cm^{-3}$. All the silicon crystals experience this temperature range during the cooling process from the melt temperature to room temperature, when oxygen becomes supersaturated and may precipitate. Fortunately, TDs can be eliminated by a heat treatment around 800ºC [36].

A second type of oxygen electrically active centres, which are known as *new donors* (NDs), are formed in the range from 650ºC to 850ºC [37]. NDs exhibit a different annealing behaviour when compared to TDs, since their generation depend on either a pre-anneal at 470ºC to 550ºC or a high carbon concentration in the silicon material ($>2\times10^{16}$) [38]. In Figure 19 is represented the formation rates of oxygen-related donors as a function of heat treatment temperature (also namely as annealing temperature).

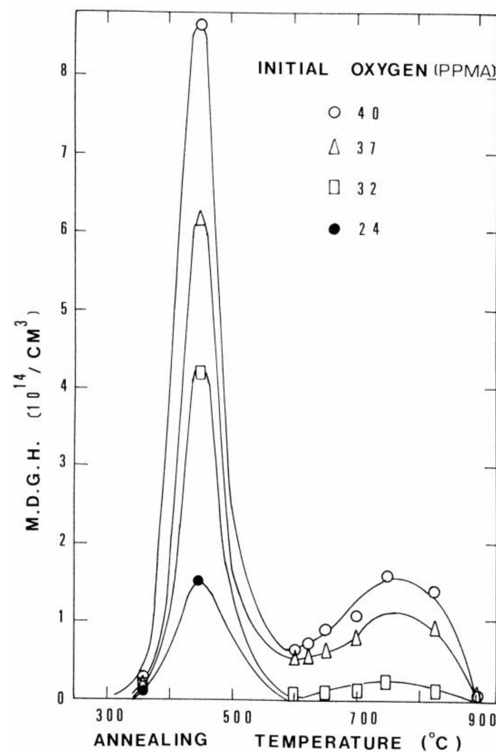

Figure 19 –Maximum oxygen-related donor generation per hour of heat treatment at given temperatures [39] – The higher peak occur at around 450ºC and corresponds to thermal donors (TDs) generation; the lower peak occur at around 750ºC and it is due to new donors (NDs) formation.

4.3. Defects in CZ silicon

As mentioned before in Chapter 3, different recombination mechanisms of holes and electrons occur at lattice defects. Several trap levels are introduced in the band gap by crystalline defects and this is the major source of efficiency losses in a semiconductor for solar cells.

Despite of crystal growth being dislocation-free, CZ silicon is not completely defect-free. Grow-in microdefects incorporated during the crystallization and cooling processes. Other crystallization imperfections in CZ silicon growth can also occur, such as impurity and dopant inhomogeneities.

The following section will present how defects are classified, the most important grown-in defects in CZ silicon, two different theories on grown-in defects formation and also the influence of impurities on their formation.

4.3.1. Defect classification

Crystal lattice defects are usually classified according to their dimension. Thus, they can be classified as point defects (0D), line defects (1D), planar defects (2D) and bulk defects (3D). The classification and overview of crystal defects in silicon lattice are shown in Table 2 and Figure 20, respectively. The categories of defects includes (i) isolated impurity atoms occupying interstitial or substitutional sites,

(ii) isolated lattice defects, i.e. vacancies or self-interstitials, (iii) aggregates of two or more impurity atoms, (iv) aggregates of two or more intrinsic defects, (v) complexes of impurity atoms with lattice defects, (vi) larger aggregates or complexes, such as precipitates, and finally (vii) dislocations [15].

The first category of defects refers to point defects (zero-dimensional defects) and includes both intrinsic and extrinsic point defects. In relation to intrinsic point defects, vacancies and self-interstitials are considered. A vacancy is formed when a silicon atom is removed from its lattice site and leaves behind four broken covalent bonds which need to be arranged in other configurations. In contrast, a self-interstital is formed when an extra atom is positioned in a lattice site that should be unoccupied in a ideal lattice structure. In relation to extrinsic point defects, these can occur unintentionally (as residual impurities) or intentionally (as dopants) and they can occupy interstitial or substitutional lattice sites [15, 40].

At crystal growth temperatures, point defects are isolated and usually electrically charged. Their charge state can lead to an interaction with electrically active dopants and, consequently, forming point defects complexes [40].

The second category of defects refers to line defects and all kind of dislocations are included, such as perfect screw and edge dislocations, mixed dislocations, partial dislocations (associated with a stacking fault) and dislocation loops. Since the lattice is only disturbed along the dislocation line, the defects are considered as one-dimensional [15, 40].

The third category of defects refers to planar defects (two-dimensional defects) which are basically represented by a disruption of the stacking of planes of atoms which forms two other common types of crystal defects, i.e., stacking fault and twins. A stacking fault can be extrinsic or intrinsic when a plane is inserted into or removed from the lattice, respectively [15, 40].

Finally, the category of bulk defects (three-dimensional defects) includes second-phase particles (precipitates), vacancy agglomerates (voids) and foreign particles (inclusions). In one hand, precipitates and voids are formed by supersaturation-driven condensation of intrinsic point defects, i.e., interstitials and vacancies, respectively. However, inclusions are melt-solution droplets, gas bubbles or even foreign microparticles incorporated at the growing melt-solid interface. In fact, these two types of defects differ in their size, where precipitates varies in the range 10-100nm and inclusions in the range 1-10μm [15, 40].

Table 2 - Classification of crystal defects in silicon [14, 41].

Point defect (0D)	Line defect (1D)	Planar defect (2D)	Bulk defect (3D)
• **Intrinsic point defect** •Vacancy •Self-interstitial • **Extrinsic point defect** •Substitucional impurity atom •Interstitial impurity atom	•**Dislocation** •Edge dislocation •Screw dislocation •**Dislocation loops** •Extrinsic type •Intrinsic type	•**Stacking fault** •Extrinsic type •Intrinsic type •**Twin**	•**Precipitate** •**Void** •**Inclusions**

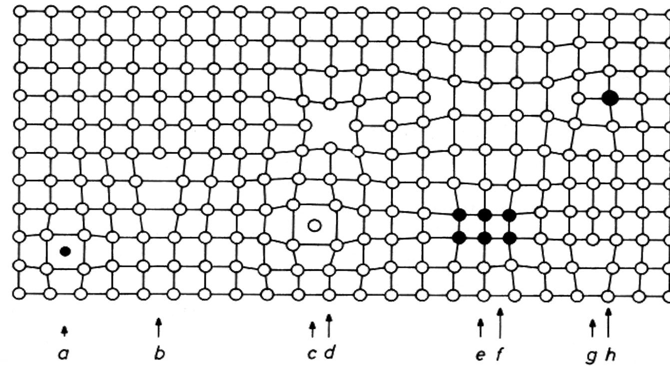

Figure 20 - Overview of crystal defects in silicon lattice [41] – a – interstitial impurity atom, b – edge dislocation, c – self-interstitial atom, d – vacancy, e – precipitate of impurity atoms, f – vacancy-type dislocation loop, g – interstitial type dislocation loop, h – substitutional impurity atom.

4.3.2. Incorporation of intrinsic point defects

There are two types of intrinsic point defects generated at the growth interface: silicon interstitials and vacancies. There are two types of theory on point defect incorporation: equilibrium theories and non-equilibrium theories. This section introduces a generally-accepted equilibrium theory – Voronkov's theory and a typical non-equilibrium theory – Abe's theory with focus on the former.

4.3.2.1. Voronkov's Theory

According to Voronkov's theory, the CZ silicon crystal is grown with vacancy or interstitial as dominant microdefect type and their formation is determined by the V/G ratio, where V is the growth rate and G is the axial temperature gradient near the solid-liquid interface of the crystal [42, 43].

In 1982, Voronkov developed an equilibrium model describing the V/G dependence. In this model is assumed that both intrinsic point defects coexist at the crystallization temperature in comparable equilibrium concentration, but vacancies concentration is still higher than interstitials [44].

This model is also based on recombination and diffusion of vacancies and self-interstitials in the vicinity of the crystal-melt interface. Upon lowering the temperature, i.e., moving away from the crystal-melt interface, both types of point defects recombine in a faster way so their concentration gradients are proportional to G. Consequently, strong concentration gradients cause their diffusion from the crystal front into the crystal bulk. Moreover, the moving crystal gives rises to the convection fluxes of the point defects proportional to V [45].

When V/G is low, i.e., when $V/G<(V/G)_{cr}$ at a sufficiently low growth rate, self-interstitials will dominate in the crystal since the prevailing flux is diffusion flux and self-interstitial are faster diffusers. Later they agglomerate into interstitial type defects (A/B-defects) [46].

For V/G above the critical value, i.e., when $V/G>(V/G)_{cr}$ at a sufficiently high growth rate, vacancies are incorporated and have higher initial concentration in the crystal since the convection flux

dominates over the diffusion flux. During the cooling, these microdefects tend to agglomerate forming larger voids. When V/G is slightly higher than the critical ratio (thus low vacancy concentration), extended defects such as vacancy-oxygen and oxygen precipitates are produced instead of vacancy agglomeration. For this reason, the main vacancy-containing region of a crystal, i.e., where voids are generated, is surrounded with a narrow marginal band containing oxide particles [46].

In addition, it is believed that *G* often increases significantly from the crystal-melt interface center to the periphery. Therefore, in the central part the *V/G* ratio will be higher than the critical value, where vacancy type defects will dominate, and in the peripheral part the *V/G* ratio will be lower than the critical value, where interstitial type defects will dominate [45, 47]. Figure 21 shows the dependence of defect pattern on *V/G* ratio.

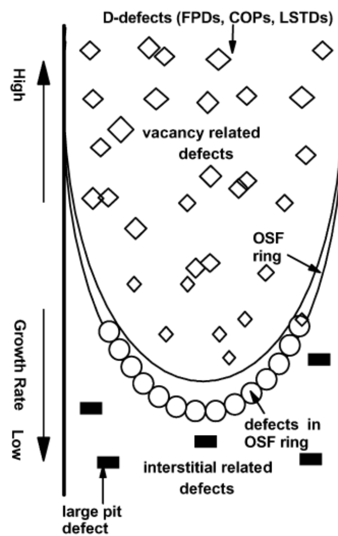

Figure 21- Illustration of the dependence of defect pattern on V/G ratio [48] - When *V/G* is below the critical value, self-interstitials will dominate in the crystal. For *V/G* above the critical value, vacancies are incorporated.

4.3.2.2. Abe's Theory

Abe et al. questioned Voronkov's model because they found that G was a decreasing function of V rather than an increasing function [49].

In this non-equilibrium model, also known as "birth and death model", the defect incorporation is believed to be only dependent on thermal gradient *G* near the interface during growth rather on *V/G* ratio. As illustrated in Figure 22, when *V* is small, *G* is large near the growth interface and the lattice contracts. Thus, excess interstitials are generated to recover the equilibrium lattice parameter. After recombination with vacancies, the rest aggregate to interstitial-type microdefects like A-defects and stacking faults on subsequent cooling. On the contrary, when V is large, G is small near the growth interface and the lattice expands. Therefore, excess vacancies are required to increase the compressive stress and shrink the lattice. During subsequent cooling, they aggregate to form vacancy-type defects (D-defects) [49, 50].

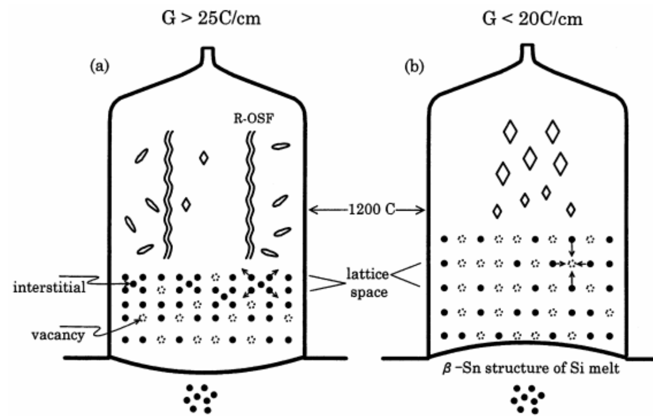

Figure 22 - Abe's proposal model on incorporation on grown-in defects in CZ crystal. Higher thermal gradient G>25ºC cm-1 (a) and lower G<20ºC (b) [49] - the defect incorporation is believed to be only dependent on thermal gradient *G* near the interface during growth rather on *V/G* ratio.

4.3.3. Different grown-in microdefects

Following the Voronkov's theory mentioned in a previous section, the defect-type will change from interstitial-type (A/B-defects) to vacancy-type (D-defects) in respect to *V/G* ratio and a defect-free gap is formed between the two regions. Since *G* often increases significantly from the crystal-melt interface center to the periphery, the radial cross section of the crystal shows a distinct defect distribution (see Figure 23) with a D-defect region in the center and A/B-defect region at its periphery [51]. In CZ-Si single crystal, the various defect regions are distinguished by their characteristics of grown-in defects. These different defect regions shown in Figure 23 will be described in the following section.

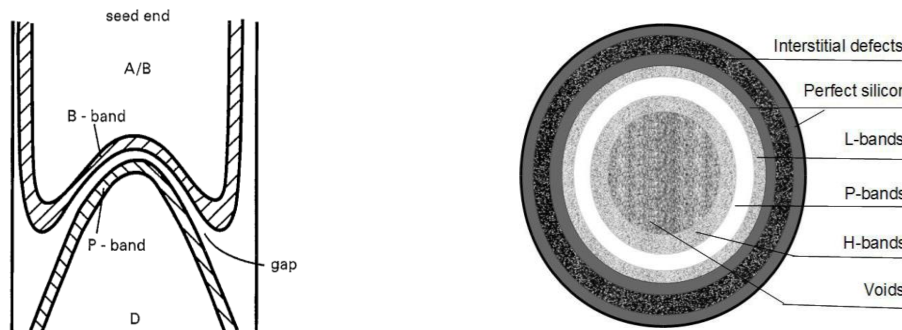

Figure 23 - Schematic spatial distribution of grown-in microdefect in an axial cross section near the critical V/G ratio and a mixed-type defects radial cross section, respectively [45, 51] - the defect-type will change from interstitial-type (A/B-defects) to vacancy-type (D-defects) in respect to *V/G* ratio and a defect-free gap is formed between the two regions. There are three distinct grown-in defect bands at the periphery of the vacancy defect region, namely P-band, H-band and L-band.

4.3.3.1. Interstitial-type defects (A/B defects)

As it was mentioned before, self-interstitials are incorporated into the crystal when $V/G<(V/G)_{cr}$ and agglomerates of excess of them into large dislocation loops are formed during the subsequent cooling

process. These defects are also referred as A-defects (or A-swirl defects) and B-defects (or B-swirls), which are represented as large and small etch pits respectively after preferential etching [52, 53]. A-defects density is generally much lower than that of the void microdefects but their size is usually orders of magnitude large, causing shorts in p-n junction [16]. This is the reason why most of CZ silicon crystals are grown in the vacancy mode, since the CZ material which is grown in interstitial mode is not suitable for electronic devices.

4.3.3.2. Vacancy-type defects: voids (D-defects)

Agglomerates of vacancies form octahedral voids and different designations are used, depending on the specific technique which was used for characterization, such as D-defects, Crystal Originated Particles (COPs) [54, 55], Flow Pattern Defects (FPD) [56] and Light Scattering Tomography Defects (LSTDs) [57, 58]. They are all D-defects or voids. For the specific case of FPD which is especially relevant for this work, a series of optical micrographs showing the nuclei site (D) and the shape of flow patterns are illustrated in Figure 24.

Yamagishi et al investigated D-defects using Secco etching and wedge-shaped ‘flow patterns’ were observed in the D-defect region for both FZ and CZ silicon wafer [56]. Later, Wijaranakula proposed a model to explain the evolution of FDPs as illustrated in Figure 24. The silicon wafers used for this experiment were chemical polished and placed vertically in the Secco etchant. Meanwhile, hydrogen gas bubbles start to nucleate at the defect site (D) and then are driven upward by buoyancy, resulting in the typical wedge-shaped flow patterns. The voids are delineated with Secco etching and they are large enough to be easily observed by light microscope. Etch pits without flow patterns are also observed and they are not related to D-defects but to crystallographic defects. These etch pits are also referred as shallow pits [59, 60].

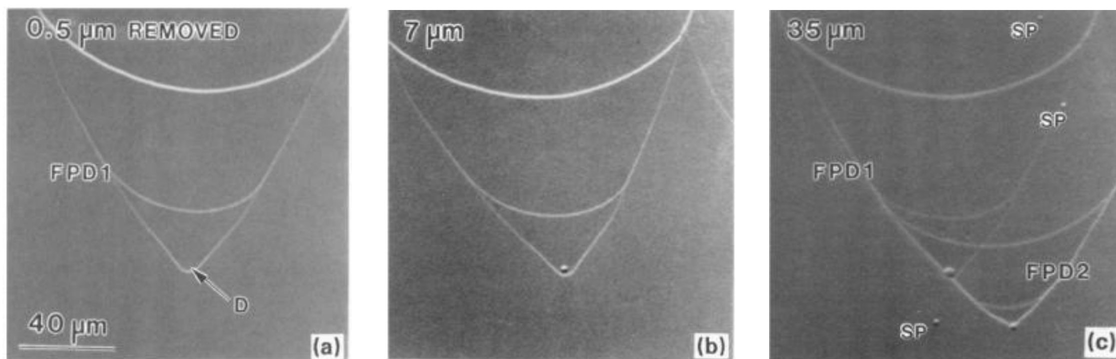

Figure 24 - A series of optical micrographs showing a flow pattern defect during a sucessive secco etching for (a) 1, (b) 14 and (c) 70 min. The amount of silicon removed is illustrated in the upper corner of each picture [59] – A FDP is shown in picture (a) but no etch pit can be seen at the nuclei site (D). In picture (b) is possible to see the void as a small etch pit. In picture (c), one more FPD is formed and some secco-etched pits (or shallow pits) are also delineated.

4.3.3.3. Vacancy-type defects: P-band, H-band and L-band

Depending on the growth conditions, the microdefects distribution can be complicated as shown in Figure 23. There are three distinct grown-in defect bands at the periphery of the vacancy defect region, namely P-band, H-band and L-band.

In the P-band instead of voids formation, vacancies tend to agglomerate with oxygen forming oxide particles (oxygen precipitates) with a typical density of 10^8 cm^{-3} [47]. This band is a very narrow region with a very low density of vacancies, since the particles consume a large number of vacancies to nucleate. Therefore, the formation ratio of particles to voids increases with vacancy concentration decreasing. The particles in the P-band are large enough to survive even at 1200ºC. If oxidation is performed, the oxygen precipitates can act as nucleation sites for stacking faults, due to interstitial which are injected from surface oxide surface, leading to oxidation-induced stacking fault rings (OiSF-ring) formation These rings are occasionally observed if the oxygen concentration is high and when seen in horizontal cuts it delineates a border between vacancy-type defects and self-interstitials regions [61, 62, 63, 64].

Silicon wafers with oxygen-related defects have a significant negative impact on the efficiency of solar cells [67]. Considering the defect nature of OiSF-rings, these regions have an important role as indicator of growth conditions and bulk properties. Therefore, the detection of these regions is of great interest for silicon industry since it can be used to optimize the useful part of the CZ crystal ingot.

In the L-band the vacancy concentration is low, resulting in a slower growth of oxide particles which starts even at low temperatures, when compared to the P-band [46]. The nucleation then proceeds in a much wider range of concentration of vacancies giving rise to a band rich in small oxide particles with a density higher than 10^{10} cm^{-3}, which can easily be dissolved at high temperature unlike the particles in P-band [64].

Finally, the H-band is a region with high concentration of vacancies when compared with that of P-band. In this band, vacancies agglomerate into voids also starting at low temperature. Therefore, vacancy consumption is limited and the residual vacancies concentration leads to a similar oxygen clustering behavior as that in the L-band, but in this case both nucleated clusters and voids coexist [45, 64].

4.3.3.4. Perfect zone

As it is shown in Figure 24, a defect-free gap is formed between A/B-defects to D-defects regions in respect to *V/G* ratio. This region is also known as "perfect zone", where interstitials and vacancies are of low concentration to promote defect nucleation [64].

4.3.3.5. Effect of impurities on microdefect formation

The formation of microdefects in CZ silicon crystals is affected by the presence of acceptor and donor impurities [66].

Impurities affect the $(V/G)_{cr}$, then the point defect incorporation, by changing the equilibrium concentrations of intrinsic point defects, trapping vacancies or self-interstitials. Both are charged point defects in silicon and the charge state is dependent on the Fermi level position [67, 68].

The equilibrium concentrations can be shifted due to Fermi level shift. When the concentration of a charged dopant is not much lower than the intrinsic electron concentration, the Fermi level will shift.

The equilibrium concentration of vacancies (negatively charged defects) will change in proportion to the electron concentration. For instant, donor dopants such as hydrogen, nitrogen and oxygen decrease the critical ratio *V/G* [68, 69, 70] expanding the vacancy region at the expense of the interstitial region. On the other hand, acceptor dopants such as boron and also carbon, increase the critical ratio *V/G* [70, 71] expanding the interstitial region at the expense of the vacancy region [67].

5. Characterization techniques

5.1. Preferential Etching

Chemical etching is widely used on silicon to remove damage layers and smooth surfaces (polishing etching or planar etching) or delineate microdefects (preferential etching or isotropic etching). The two different etching processes are illustrated in Figure 25.

A typical isotropic etchant solution includes an oxidant, a dissolving agent (HF) and a diluent. In this case, silicon is oxidized by an oxidant followed by the dissolution of the oxide which is formed. Therefore, typical etchant contains a strong oxidizing agent such as nitric acid (HNO_3), and hydrofluoric acid (HF) as a dissolving agent [72].

The defect delineation process depends on silicon surface crystallographic orientation, type of dopant, dopant concentration and composition of etchant used. Thus, different chemical solutions such as Secco, Wright, Yang, Sopori, Dash, Sirtl, Shimmel, etc, are commonly used for silicon defect delineation.

Since holes are required for the oxidation of silicon, for n-type material the surface etching is accentuated in the presence of light due to generation of electron-hole pairs. In contrast, the effect of chemical etching on p-type silicon surface is small.

The reaction rate differs locally in the presence of inhomogeneities and defects, the etch rate will equally varies. These variations will produce a non-planar etched surface that reflects the distribution of inhomogeneities and defects on the sample surface. The formation of a non-planar etched surface is mainly due to strain field associated to the presence of those defects. This strain field produces surface potential at the site of microdefects and in turn it causes a difference in the etching rate. The microdefects will thus be delineated as etch pits [73].

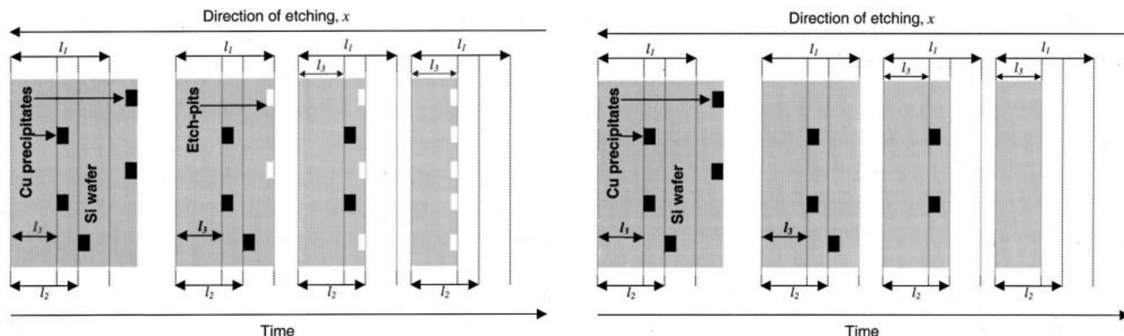

Figure 25 - Illustration of the processes of preferential etching and polishing etching, respectivley [72] – preferential etching delineates microdefects while polishing etching removes damage layers and smooth surfaces.

5.2. Lifetime Measurement Methods

There is three different measurement modes: steady-state technique such infrared lifetime imaging (ILM) [74] quasi-steady-state techniques such as QSSPC [75] and CDI [76]; and transient techniques such as microwave detected photoconductance decay (MWPCD) [77]. The steady-state and QSS techniques are in principle measuring actual lifetime, whereas the transient technique is generally only measuring differential lifetime [78, 79].

In this section, PL technique, which was the only used in this thesis work used for measuring material lifetime, will be introduced.

5.2.1. Photoluminescence Imaging (PL)

This characterization technique is based on mapping photoluminescence (PL) intensity from silicon material. As a result, spatially resolved calibrated minority carrier lifetime and series resistance measurements are performed [80, 81].

In luminescence imaging of silicon samples, the entire sample area is excited by optical excitation using a laser and a beam expander. The resulting variation in PL-emission is measured with a CCD-camera resulting in a final image [80, 81].

This technique detects band-to-band emission from the sample at room temperature, which is a wide spectrum with a peak at about 1140 nm [81]. Thus, PL imaging results from radiative recombination of photogenerated charge carriers. The intensity of this band-to-band PL signal scales with the number of (photo-) excited minority charge carriers. The measurement is carried out during steady-state photoexcitation, such that spatial variation in intensity across the sample state photoconductance calibration measurement is carried out to convert the PL intensity to absolute charge carrier density. This allows qualitative lifetime measurements [80].

Recently, lifetime images were obtained by calibration with other lifetime measurement techniques such as infrared lifetime mapping/carrier density imaging (ILM/CDI) or by QSSPC measurements. However, the comparison for the calibration in these methods is done at different excitation conditions and therefore for different carrier density profiles, leading to significant systematic errors. More recently, a solution was proposed by integrating a QSSPC system into a PL imaging setup as demonstrated in Figure 26 [82].

The rate of radiative recombination $\mathrm{R_{rad}}$, and therefore the PL signal $\mathrm{I_{PL}}$, is proportional to the product of the electron and the hole carrier densities. For a p-type Si wafer of doping concentration $\mathrm{N_A}$, a quadratic dependence on the excess carrier density Δn is expected for the PL signal:

$$I_{PL} \propto R_{rad} \approx B.\Delta n(\Delta n + N_A) \quad (3)$$

where B is the radiative recombination effect [82].

The major advantages of using PL imaging are the possibility to monitor the processing of solar cells at any stage of fabrication because no electrical contacts are required. However, one general disadvantages of PL imaging compared to e.g. QSSPC technique is that the calibration of the measured signal into an absolute excess minority carrier concentration varies strongly form one sample to the next. This is mainly because the calibration depends on the sample geometry and on the doping concentration [84]. Another disadvantage is that this technique requires a separate calibration measurement to convert from PL intensity to carrier density and thus lifetime. Knowledge about samples reflectance and doping is necessary [80].

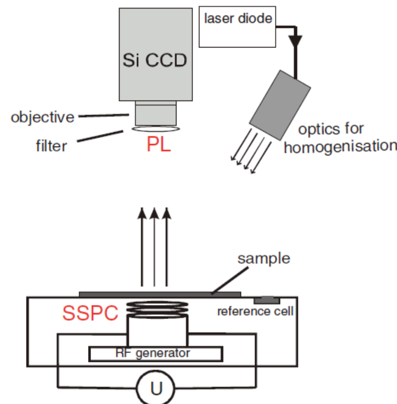

Figure 26 - Typical illustration of an experimental setup for photoconductance-calibrated photoluminescence lifetime imaging - the entire sample area is excited by optical excitation. The resulting variation in PL-emission is measured with a CCD-camera resulting in a final image [82].

5.3. Fourier-Transform Infrared Spectroscopy (FT-IR)

This analytical technique measures the absorption of infrared light (IR) and provides specific information about bond concentration and other molecular structures.

When the sample is exposed to IR radiation, chemical bonds which vibrate at specific frequencies will absorb the radiation at frequencies that match with those ones. As a result, a spectrum of radiation absorption as a function of frequency can be obtained. The resulting integrated peak area is proportional to bond concentration. The peak sizes are a direct indication of the impurity concentration in the material [80].

As it is represented in Figure 27, a Fourier-transform (FT) spectrometer consists of an infrared light source, moving and stationary mirrors, a beam splitter and a detector. First, the incident infrared light on the beam splitter is reflected from both mirrors direction, then transmitted again to the beam splitter where they are recombined and transmitted to the detector.

During the sample analysis process, all frequencies are being measured simultaneously and the interference between the lights reflected from both mirrors generates an interferogram. This is a modulated radiation signal as a function of the displacement of the moving mirror. Then, this signal is transmitted to the detector which encodes the wavelength or wave number information from the source radiation. The quantification of bond concentration is performed using Fourier transformation [84, 85].

FTIR is commonly used for qualitative analysis, so for quantitative measurements, Beer-Lambert law is followed:

$$A = abc \quad (4)$$

Where *A* is the absorbance, *a* is the absorptivity, *b* is the thickness or path length and *c* is the concentration. The thickness and absorptivity are constants, while the absorbance will be determined using FTIR. Thus, the impurity concentration is calculated [84].

It is very common to use this technique for determining the interstitial oxygen (O_i) and substitutional carbon (C_s) concentration in silicon since they have specific absorption peaks at 1107cm^{-1} and 605cm^{-1}, respectively [80].

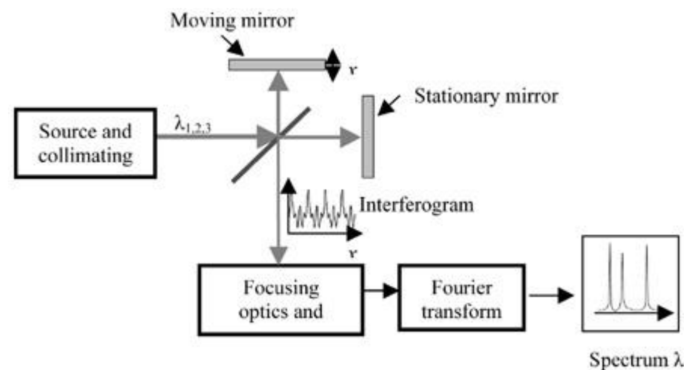

Figure 27 - Shematic of sample analysis process by FTIR [85] - the infrared light is collimated and directed to a beam splitter. The light is refracted towards towards the fixed mirror and transmitted to the moving mirror. All frequencies are being measured simultaneously and the interference between the lights reflected from both mirrors generates an interferogram. This signal is then transmitted to the detector which encodes the wavelength. The quantification of bond concentration is performed using Fourier transformation.

5.4. Four point probe (FPP)

The four point probe is used to measure the material resistivity by passing a current (*I*) between two outer probes and, simultaneously, measuring the voltage (U_V) between two inner probes (see Figure 30) [80].

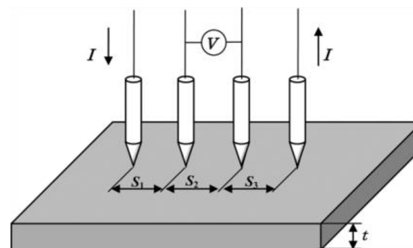

Figure 28 - Schematic of four point probe [86] – there is two electrodes which supply current and other two which measure voltage.

The distance from any probe to the nearest edge is at least four times the probe spacing, which is normally equals to 0.635mm (namely *d* or *s*). For a thin sample with the thickness t below 5d, the resistivity is given by [64]

$$\rho(\Omega.cm) = \frac{2\pi d U_V z}{I} \tag{5}$$

Where z is the thickness correction factor given by [64]

$$z = \frac{1}{1 + \frac{0.52632}{(t/d)^{1.9}}} \tag{6}$$

In the case of measuring the resistivity of a non-compensated semiconductor, that will reflect both the concentration of dopant and TD if it is present in the material.

5.5. Light microscope

In this technique a silicon sample surface is illuminated by ordinary illumination and a magnified picture is produced by the reflected light through the use of lenses. The presence of defects can be studied using the light microscope [81]. A simplified schematic drawing of the optical path of a light microscope is shown in Figure 29.

The illumination from a light source is collimated by the condenser lens to form an image of the light source in the back focal plane of the objective lens, in order to illuminate the sample with near parallel light. The light scattered by the sample is captured by the objective lens and produces a magnified image of the sample in the image plane. This image is further magnified by the ocular or eye piece. A microscope contains several interchangeable objective lenses and that are used to magnification of e.g. between 2.5x and 100x. The ocular has a fixed magnification of e.g. 10x, and the total magnification is then between 25x and 1000x [81].

The system is also connected to a camera and a computer making it possible to take images by using appropriate software (ImageAccess easyLab 7 was the software used in this thesis work).

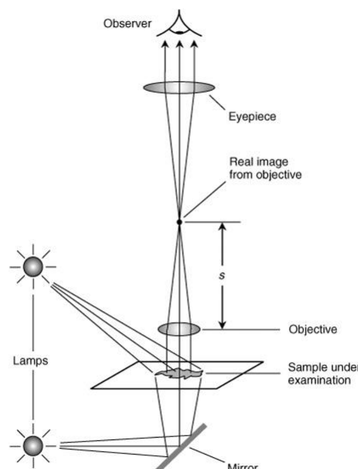

Figure 29 - Simplified schematic drawing of the optical path of a ligh microscope in reflection mode [87] - the sample surface is illuminated and a magnified picture is produced by the reflected light through the use of lenses.

6. Experimental details

In this chapter, experimental details of this thesis work will be given. Prior to any kind of measurement, silicon as-grown samples require an appropriate preparation. Therefore, the first section will be about samples preparation. After this process step, it was possible to perform oxygen and resistivity measurements. The second section is then dedicated to this subject. In order to proceed with TDs annihilation, a rapid thermal process (RTP) oven was used, so there will also be a section about how the procedure was carried out. Subsequent to TDs dissolution, oxygen and resistivity measurements were performed again in order to calculate the TDs concentration. Final lifetime measurements were obtained. On the other hand, parallels samples were also prepared to delineate crystal defects in order to study them by using optical methods such as light microscope. Two sections about defect etching and light microscope observations will be also given in this chapter. A flow chart of the measurements performed is illustrated in Figure 30.

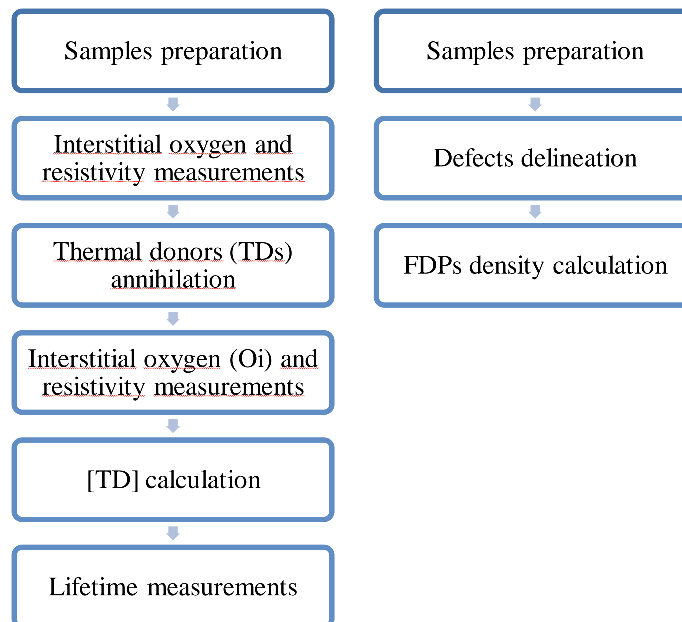

Figure 30 – Flow chart of measurements performed in this thesis

6.1. Samples

For the purpose of this work, four n-type CZ silicon ingots with different tapered angle and shouldering area were characterized. A p-type CZ silicon ingot was also characterized in order to do some comparisons.

The different crowns were grown in the same crystal pull speed, undercooling rate and heat power temperature reduction conditions conditions until it reaches a certain diameter before the shouldering step starts. In fact, these parameters change from ingot to ingot during the shouldering step, since it is the operator who controls the process. Therefore, the growing time changes and, consequently, the transition area. The transition area and growing time for all CZ-Si samples investigated is given in Table 3. In addition, differences in the crowns shape, i.e., crown tapered angles, were found even if the

crystal pull speed was kept constant in its formation. The crown tapered angle for all samples and the respective growing time are given in Table 4.

Table 3 - Transition area (or shoulder area) and correspondent growing time for all samples under investigation.

Sample	Transition area (mm^2)	Growing time (min)
C1N	2760	24
C2N	1870	13
C5N	3010	25
C6N	3370	27
C2P	1870	13

Table 4 - Crown tapered angle and correspondent growing time for all samples under investigation

Sample	Tapered angle (°)	Growing time (min)
C1N	36.1	109
C2N	33.7	101
C5N	39.0	117
C6N	36.3	109
C2P	33.7	101

Substantial differences between samples radius as a function of sample length can be observed, as illustrated in Figure 31. Those differences basically reflect fluctuations on the thermal history during the growth process. It could be explained by the existing difference on the melt temperature before the crown formation. Though, this subject is not the real motivation of this work.

Differences on absolute lifetime between samples were observed, as illustrated with PL imaging in Figure 32. Not to mention the relationship between samples area (crown and shoulder), growing time and lifetime, represented in Figure 33. Higher the growing time, higher the sample area and also the lifetime. Also, the relationship between lifetime and crown tapered angle, represented in Figure 34. The crown with the higher tapered angle has also the higher lifetime. In contrast, the crown with the lower crown tapered angle has the lower lifetime.

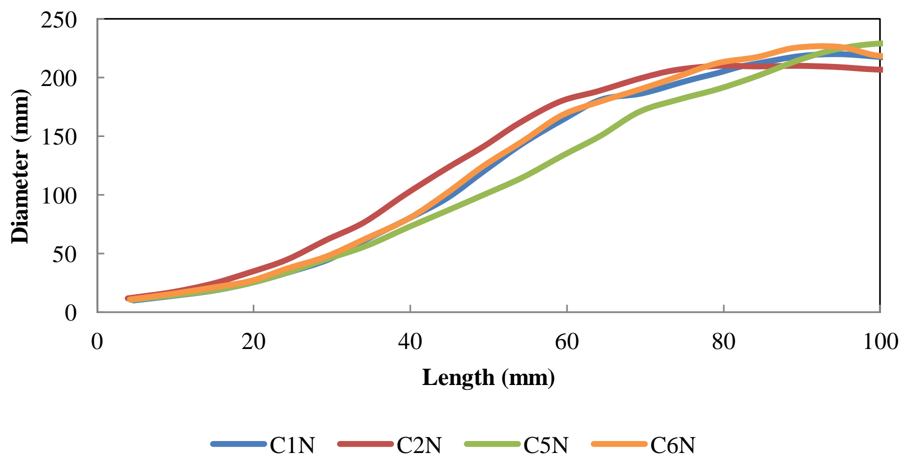

Figure 31 - Sample diameter as a function of length for all samples investigated.

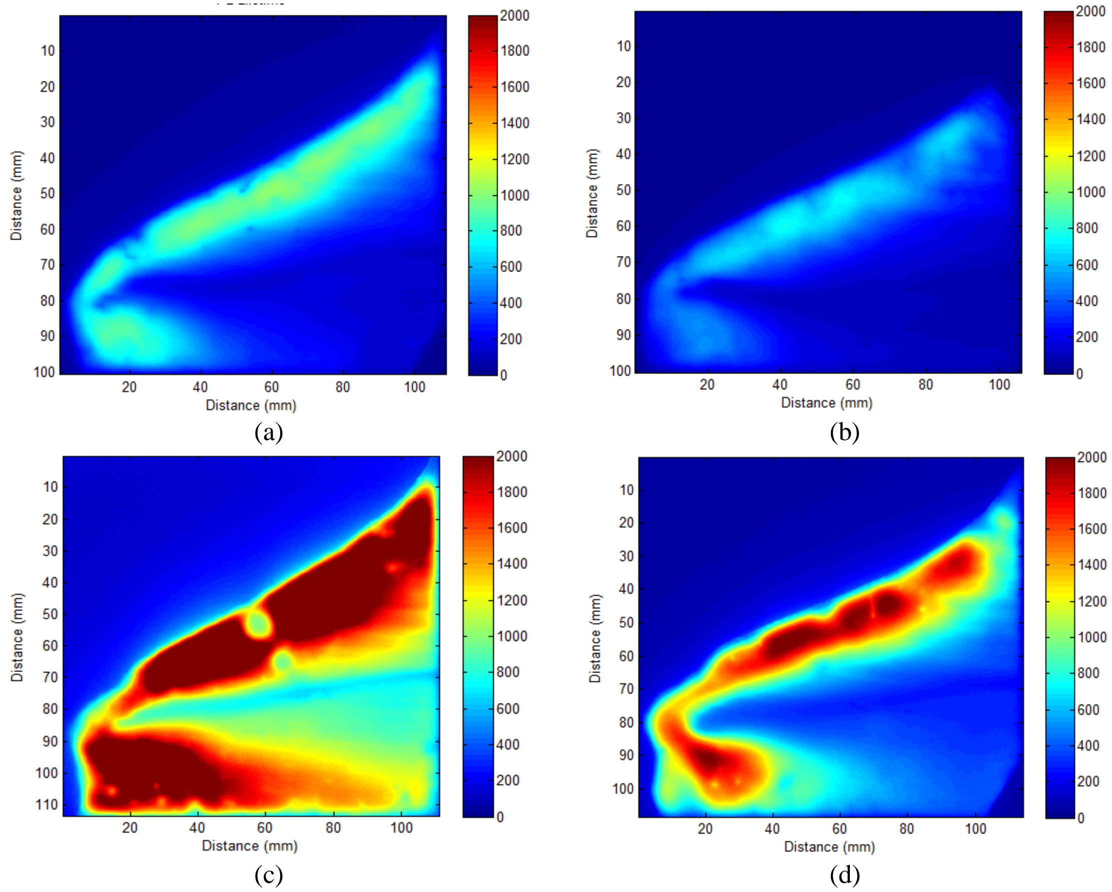

Figure 32 – Lifetime (µs) measurements with PL imaging of the sample (a) C1N, (b) C2N, (c) C5N and (d) C6N under as-grown conditions - The crown with the higher tapered angle (C5N) has also the higher lifetime. In contrast, the crown with the lower crown tapered angle (C2N) has the lower lifetime.

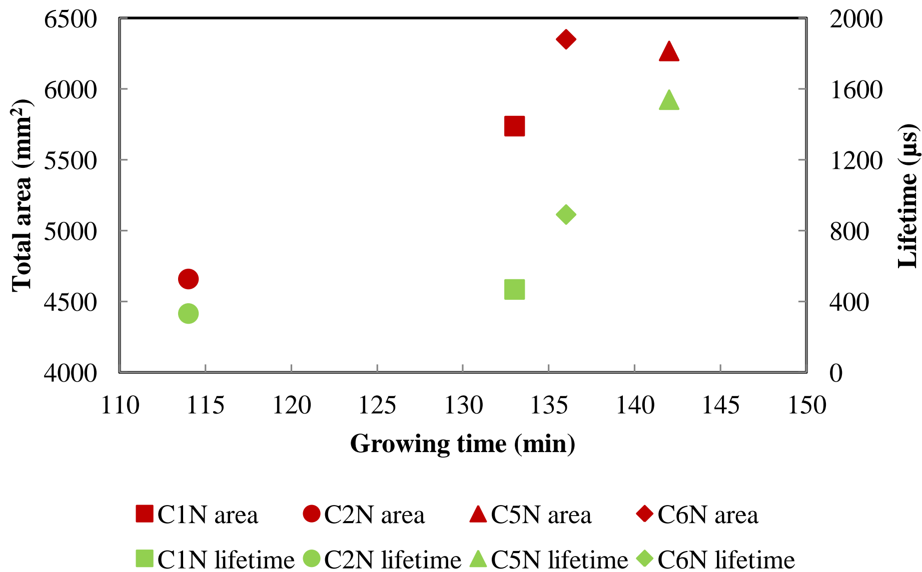

Figure 33 - Samples area and average lifetime as a function of the growing time (crown and shoulder).

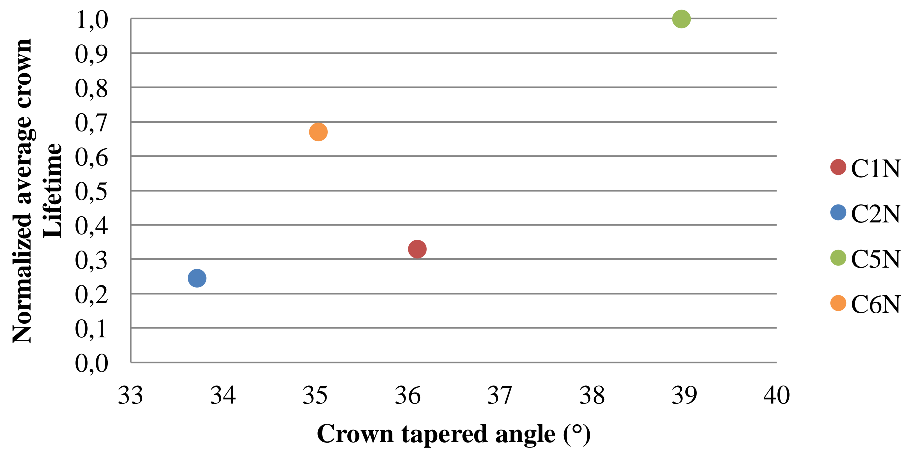

Figure 34 - Normalized average crown lifetime as a function of crown tapered angle – the relationship between lifetime and crown tapered angle is almost exponential.

6.2. Samples preparation

Sample preparation includes mechanical polishing, a cleaning process and chemical polishing (and the details are given in Figure 35).

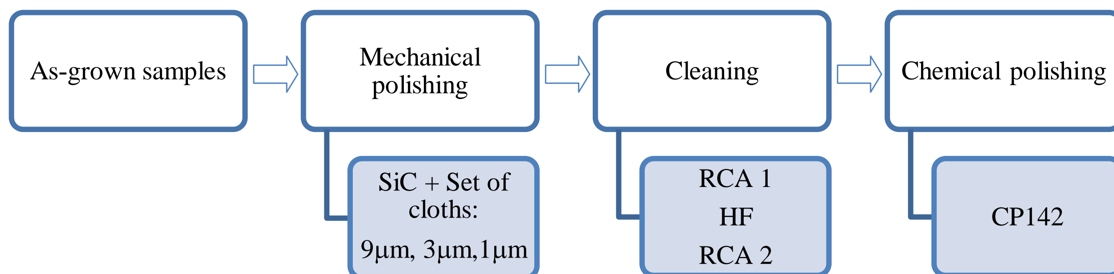

Figure 35 - Schematic view of the samples preparation steps

Silicon as-cut samples require a mechanical polishing step before being cleaned and chemical polished, in order to remove surface sawing damages and to obtain a mirror-like surface effect. For this purpose, an automatic polishing machine was used with a first step of SiC paper 1200 grit and thereafter with a set of three cloths with different grain size. Each different cloth requires a specific time. In this thesis work, the set of cloths used was: 9µm (4min + 3 min), 3µm (4 min + 3 min) and 1µm (3 min + 3 min).

Subsequent to mechanical polishing, the removal of particles and impurities from the sample surface needs to be performed. Thus, the standard cleaning method (RCA) was used and three steps are performed: removal of organic contaminants (RCA-1), oxide removal followed by removal of metallic contaminants (RCA-2). The RCA-1 solution contains ammonium hydroxide (NH_4OH) with 28% of concentration, hydrogen peroxide (H_2O_2) with 30% of concentration and deionized water (DI water), in a ratio of 1:1:5. The samples were immersed in this solution, which was heated until 75-80ºC, for 10 min, followed by a rinse in DI water. The oxide formed by this step is subsequently removed in a

hydrofluoridric acid (HF) solution with 5% of concentration, followed again by a rinse in DI water. The RCA-2 solution contains hydrogen chloride (HCl) with 27% of concentration, hydrogen peroxide (H_2O_2) with 30% of concentration and deionized water (DI water), in a ratio of 1:1:6. The samples were immersed in this solution, which was heated until 75-80ºC, for 10 min, followed by a rinse in DI water.

Finally, after the cleaning process the samples are chemical polished in order to remove a few layers of material to eliminate remain contaminants. The chemical polishing solution used was the CP142 which includes HF with a concentration of 48%, nitric acid (HNO_3) with a concentration of 65% and acetic acid (CH_3COOH) with a concentration of 100%, in a ratio of 1:4:2. A schematic of the cleaning process and chemical polishing is represented in Figure 36.

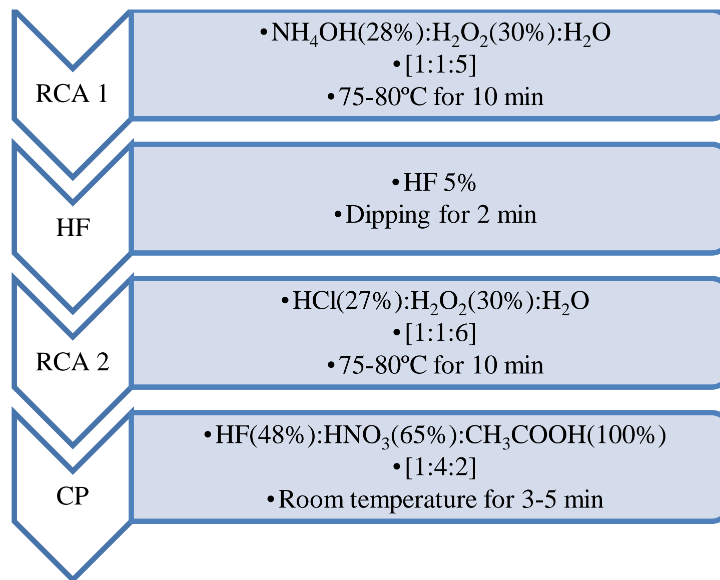

Figure 36 - Cleaning process steps and following sample chemical polishing.

6.3. Oxygen and resistivity measurements procedure

Interstitial oxygen and resistivity were measured using FTIR and four-point probe techniques, respectively. Both interstitial oxygen and resistivity measurements followed the same procedure. Six vertical lines with different distance between each other were followed. For each line, the measurements were carried out with 2mm of resolution. However, in the case of resistivity measurements the distance from any probe to the nearest edge is at least four times the probe spacing [89] so there is less number of points comparing to that of oxygen measurements. The measurement procedure was the same for all samples and the distance between measurement lines was the same ratio between each line radius and sample radius, then is possible to compare the outcomes between samples. An illustration about oxygen and resistivity measurements procedure is represented in Figure 37.

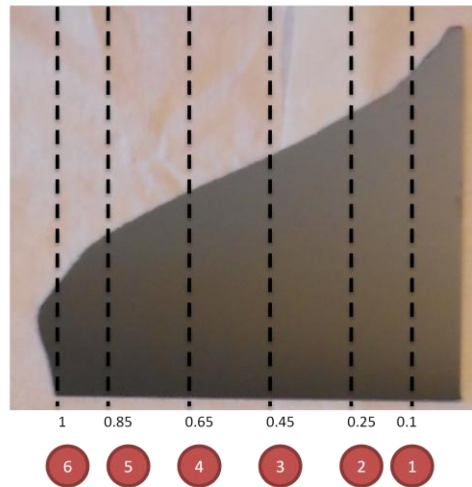

Figure 37 - Illustration about oxygen and resistivity measurements procedure - Six vertical lines followed. For each line, the measurements were carried out with 2mm of resolution.

6.4. Rapid Thermal Process (RTP) oven

In order to proceed with TDs annihilation, a rapid thermal process (RTP) oven was used. First, a cleaning step was performed, since it is necessary to have a very clean environment inside the oven, free of possible remained contaminants from other experiments which were carried out before. The cleaning steps are shown in Table 5. First, for 6 minutes the oven is at 25ºC. Then, the temperature increases with a ramping rate of ~7ºC/s until 200ºC, where it stays for 30 seconds in order to prevent a thermal shock in the lamps. After, the temperature increases again with a ramping rate of 50ºC/s until 800ºC, where it remains for 5 minutes. Finally, the system cools down with a cooling rate of ~1ºC/s until it reaches 25ºC again.

Thus, after the cleaning step the sample is introduced inside the oven. The sample is placed on the top of a p-type Si carrier which is just one-side polished. A thermocouple is attached to the Si carrier in order to control the sample temperature during the experiment. The TD annealing steps are shown in Table 6. First, for 2 minutes the oven is at 25ºC. Then, the temperature increases with a ramping rate of 5ºC/s until 150ºC. Immediately after, the temperature increases again with a ramping rate of 50ºC/s until 800ºC, where it stays for 15 seconds. In fact, an annealing at 800ºC for 10s [89] is enough to dissolve the TDs, still 5 seconds were added to the total time as an “error coefficient” to be sure that the sample would not be subject to this temperature for less than 10s. Finally, the system cools down with a cooling rate of 1ºC/s until it reaches 25ºC again.

Table 5 - RTP oven cleaning steps

Step	1	2	3	4	5	6	7	8	9	10	11	12
Temperature (ºC)	25	25	25	25	25	25	200	200	800	800	25	25
Time (s)	60	60	60	60	60	60	30	30	16	300	26	120
N_2 (sccm)					500		500	500	500	500	500	500
Close primary vacuum valve												
Open purge valve				yes		yes						

Table 6 - Thermal donor annihilation steps using a RTP oven

Step	1	2	3	4	5	6	7	8	9
Temperature (ºC)	25	25	25	25	150	800	800	25	25
Time (s)	30	30	30	30	30	16	15	25	300
N_2 (sccm)					500	500	500		
Close primary vacuum valve	yes		yes		yes	yes	yes		yes
Open purge valve	yes		yes						yes

6.5. Defect etching

As it was mentioned in section about Preferential Etching, several etchings can be used to delineate crystal defects in order to study them by using optical methods such as light microscope.

Prior to defect etching, the samples were polished and cleaned. In order to delineate FDPs, Secco etching was performed. Its composition includes HF with a concentration of 48%, potassium dichromate ($K_2Cr_2O_7$) and DI water in a ratio of HF:H_2O = 2:1 where 44 g $K_2Cr_2O_7$ are first dissolved in 1 liter of DI water. The samples are then immersed in the solution for 30 min without agitation. Etch pits on all crystallographic planes are developed.

Since this etchant contain Chromium, it will contaminate the samples which turn to be not useful anymore after defects observations on light microscope, except for FTIR measurements.

6.6. Light microscope observations

Light microscope observations followed the same measurement procedure of oxygen and resistivity. Six vertical lines with different distance between each other were followed. The sample was placed in a moving stage and the measurements were performed with both 1mm and 2mm of resolution to verify which resolution could be better for further measurements. During this work, the light microscope model used was Leica MEF4M.

6.7. Lifetime measurements

In order to obtain sample lifetime measurements after TDs dissolution, samples were first etched for 90 seconds in a CP5 solution and cleaned using Piranha and HF. Then, samples were double-side passivated in a PECVD chamber with a-Si: H and annealed for 1 min at 450 °C. Lifetime was measured with Photoluminescence. Both processes were performed in IFE (Institute for Energy Technology at Kjeller in Norway).

7. Results

CZ-Si samples were characterized in terms of lifetime, resistivity, interstitial oxygen and TDs concentration. FDPs were counted and the defects nature evaluated by light microscope observations. In this chapter, all the results will be given.

7.1. Flow pattern defects (FPD) calculation method

In Figure 38, light microscope images show the FPD which were delineated by using Secco etching. In Figure 38 (a), the FPD density calculation method is illustrated and this just takes into account the presence of D-defects. In Figure 38 (b), an illustration of the D-defect, FPD and shallow pits (SP) is shown.

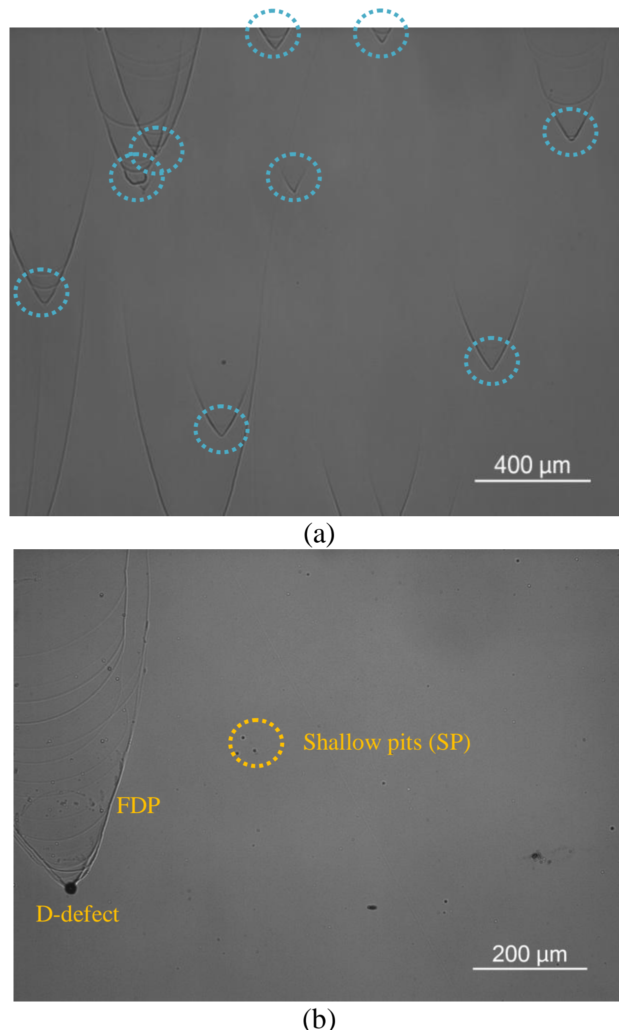

Figure 38 – Light microscope images (a) The FPD density calculation method with 50x magnification and (b) Ilustration of D-defect , FDP and shallow pits (SP) with 100x magnification.

7.2. Light microscope sensibility test

In Figures 39 and 40, a light microscope sensibility test is shown. That was performed for the first vertical line with 50x and 100x of magnification to determine which resolution would be better suited for further measurements. Significant variation in FPD density is evident between different magnifications. Two possible reasons are related to the manual sample movement and non-intentional plate movements, which is illustrated in Figure 41. Note that the horizontal axis represents the normalized sample length in relation to the shoulder starting point.

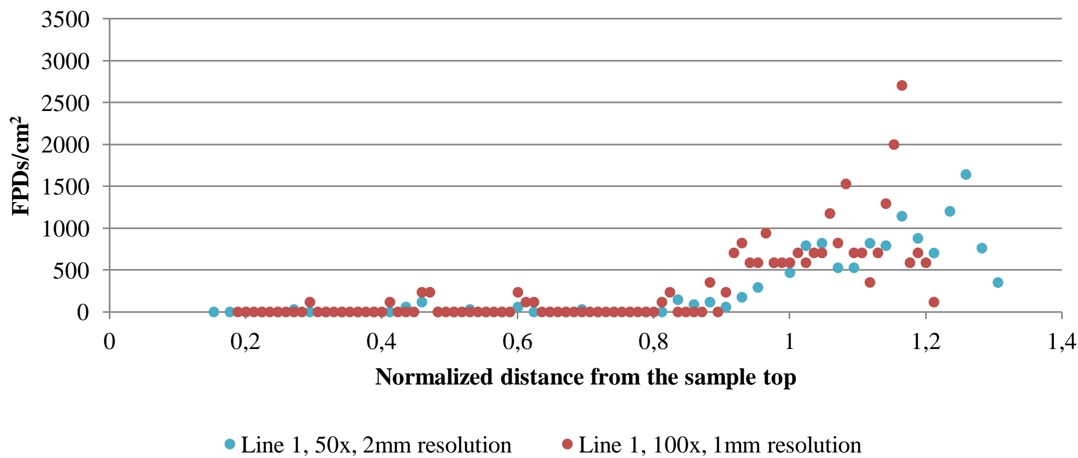

Figure 39 – FPD distribution for Line 1 of sample C5N following two different resolutions

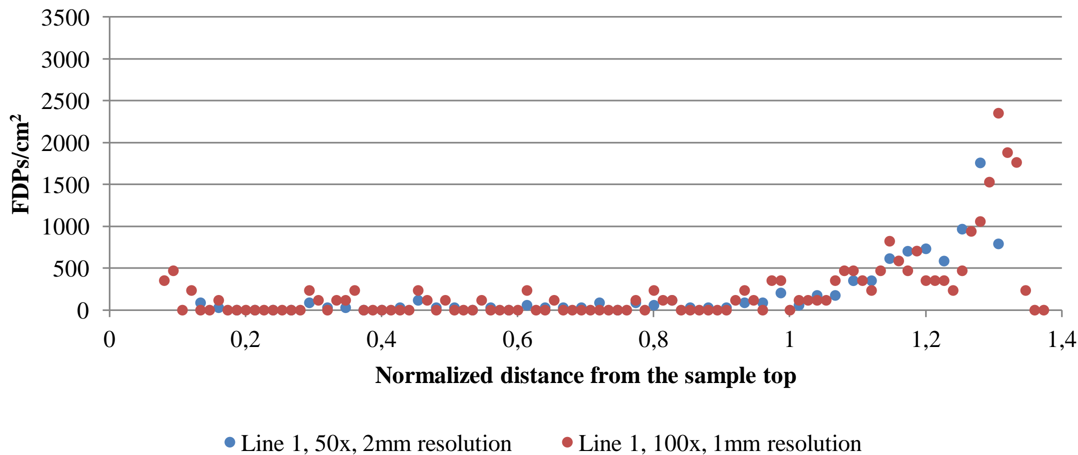

Figure 40 – FPD distribution for Line 1 of sample C6N following two different resolutions

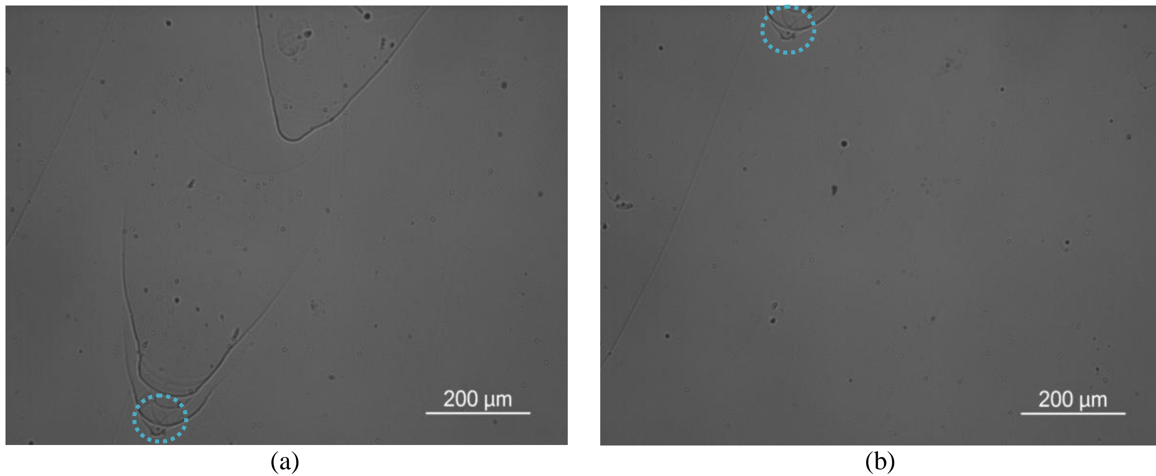

Figure 41 – Example of the possible FPD counting repetition due to manual sample movement.

7.3. FPD density and P-band position

In Figures 42 and 43, FPD density along the first line measured as a function of sample length for all samples is illustrated. The respective P-band position is also represented. In Figure 42, C5N shows a higher FPD density in V-region compared to C2N and a higher drop on FPD density is observed for the first one when the early body starts. In Figure 43, C1N shows higher FPD density in V-region but the sample C6N reaches a higher peak followed also by a higher drop in the beginning of the early body.

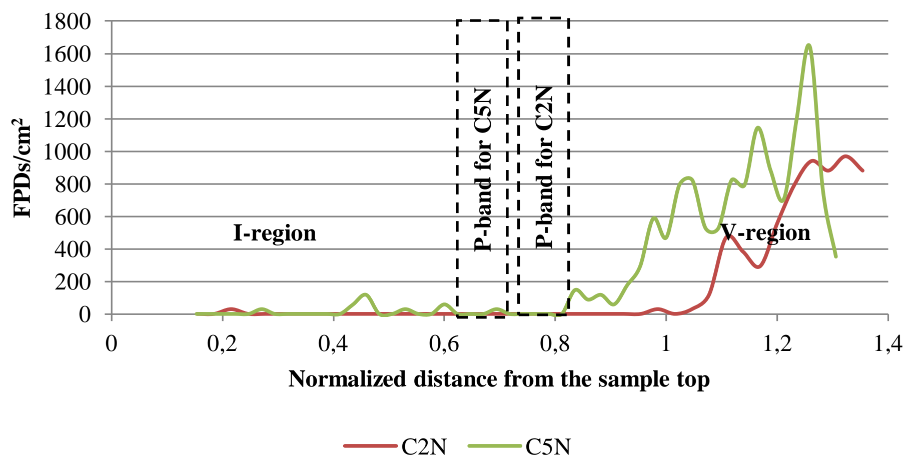

Figure 42 - FPD density along the first line measured (ingot center) as a function of sample length of samples C2N and C5N, with 2 mm of resolution. The respective P-band position is also represented.

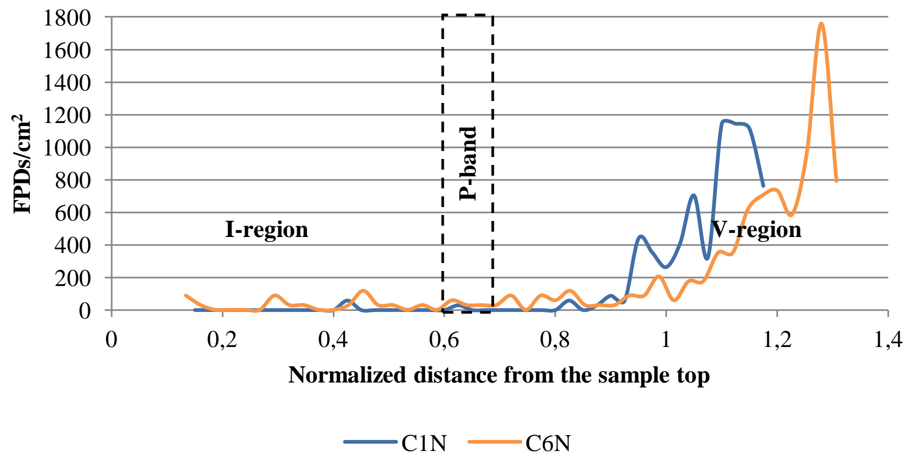

Figure 43 - FPD density along the first line measured (ingot center) as a function of sample length of samples C1N and C6N, with 2 mm of resolution. The respective P-band position is also represented.

Light microscope pictures from different regions, before and after transition, are illustrated in Figure 44 and 45, respectively. Before transition no defects are found or they density is too low. After transition, C2N shows the lower FPD density and C5N the higher. Comparing C1N with C6N, for a similar sample length, the FPD density is coincidently similar.

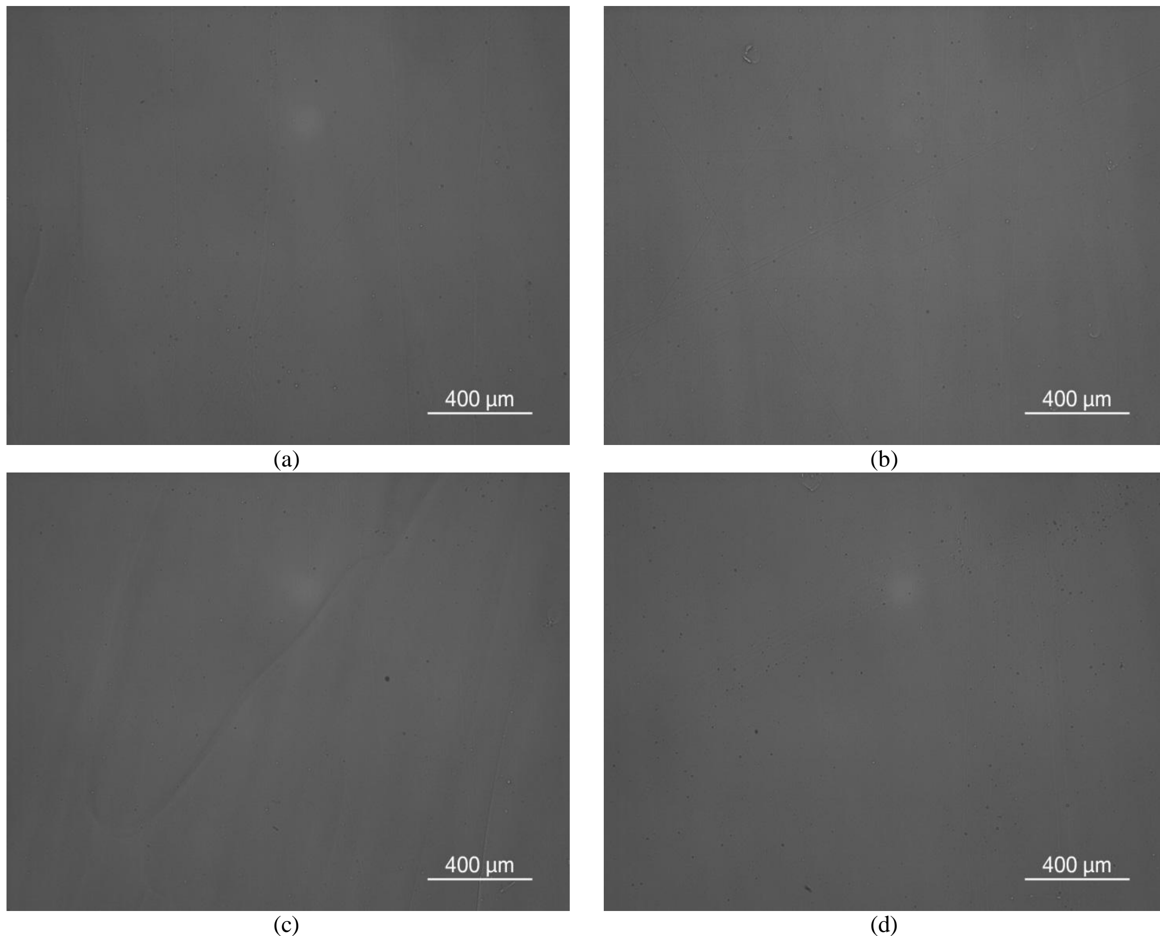

(a) (b) (c) (d)

Figure 44 - Light microscope pictures before transition for (a) C1N, (b) C2N, (c) C5N and (d) C6N.

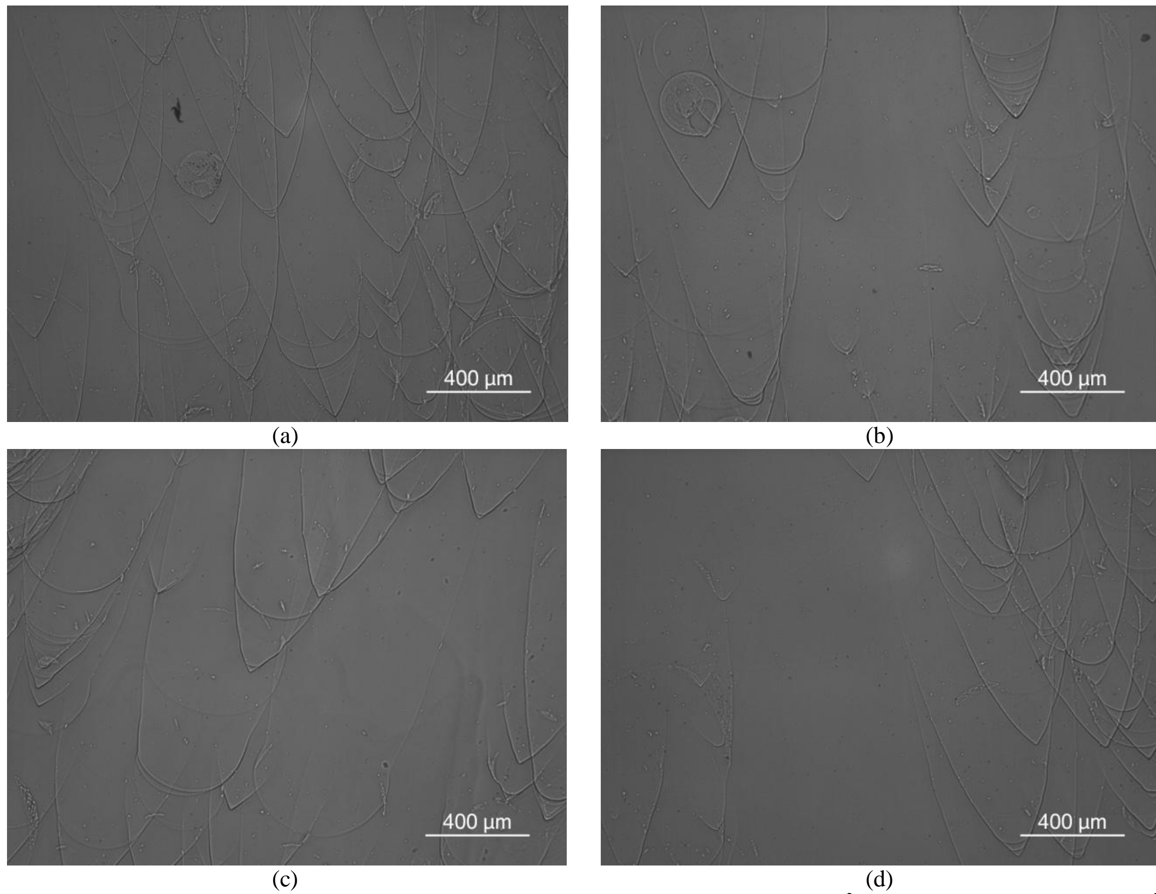

Figure 45 - Light microscope pictures after transition for (a) C1N with 733 FPD/cm^2 , (b) C2N with 557 FDPs/cm^2 , (c) C5N with 704 FPD/cm^2 and (d) C6N with 733 FPD/cm^2.

7.4. Oxygen measurements in as-grown conditions

In Figure 36, interstitial oxygen measurements along six vertical lines as a function of the sample length are illustrated for all samples. Generally, the oxygen concentration decreases from the ingot center towards the edge, where line 1 represents the closest line to the center and line 6 the closest line to the edge. The maximum concentration is obtained when the sample diameter is also at its maximum.

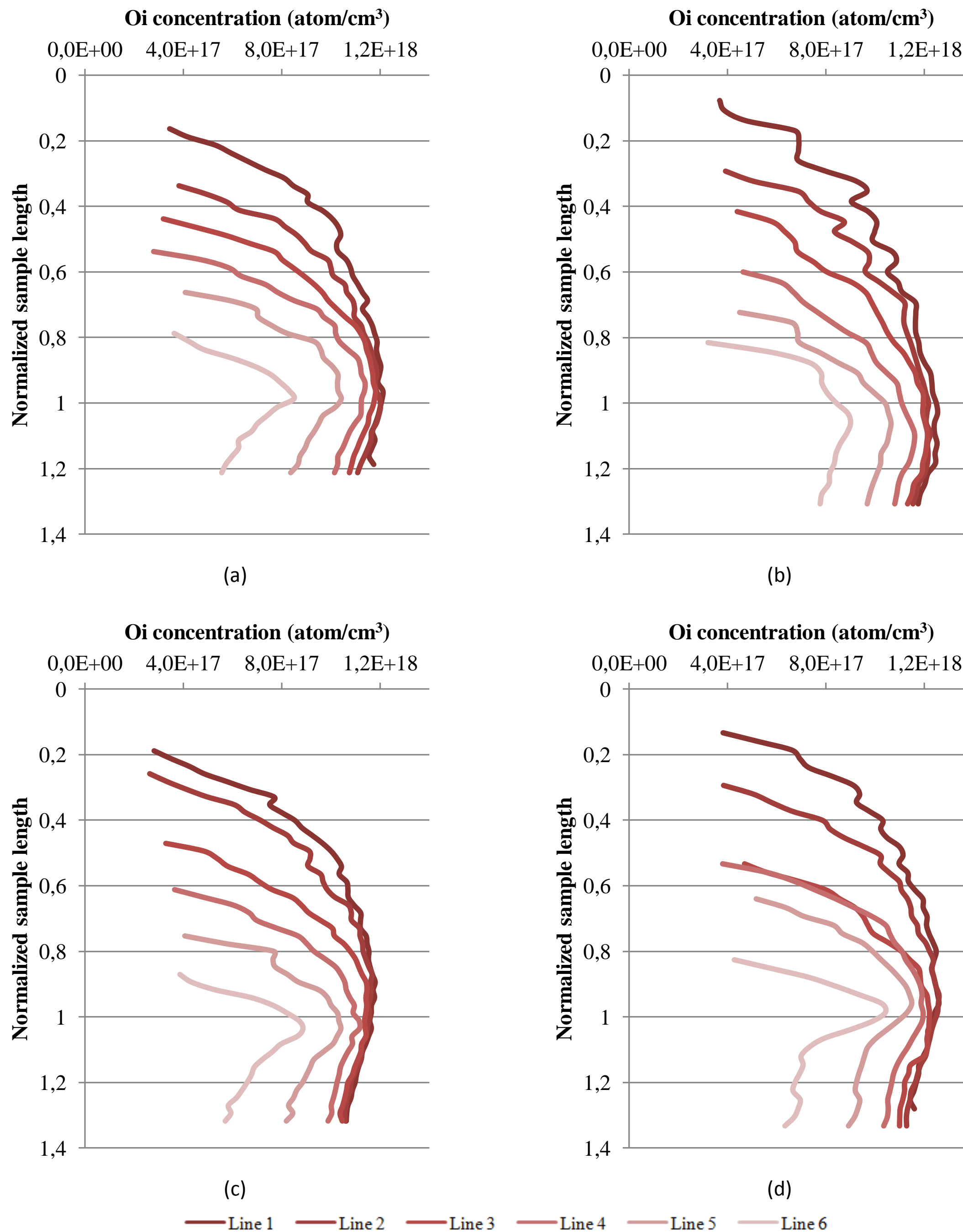

Figure 46- Interstitial oxygen measurements along six vertical lines as a function of the sample length for (a) C1N, (b) C2N, (c), C5N and (d) C6N in as-grown conditions.

In Figure 47, interstitial oxygen measurements along the first vertical line as a function of the sample length for all samples in as-grown conditions are shown. The interstitial oxygen distribution increase along this part of ingot until it reaches a maximum point followed by its discrete decreasing. In the crown region, C2N has higher oxygen concentration compared to C5N. The samples C1N and C6N represent the middle situation. In Figure 48, the same is illustrated, but just for the early body region. The sample C2N has a lower decreasing rate of the oxygen concentration when compared to that of C5N and C6N.

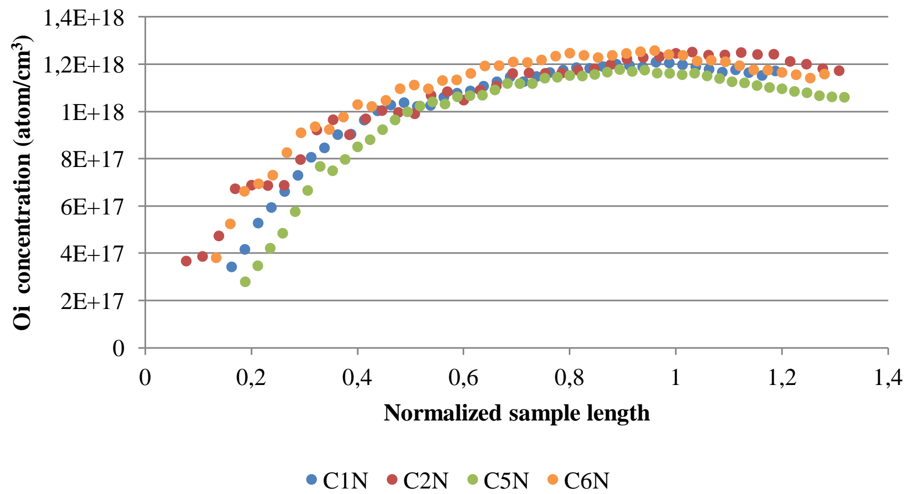

Figure 47 – Interstitial oxygen measurements along the first vertical line (ingot center) as a function of the sample length, for all samples in as-grown conditions .

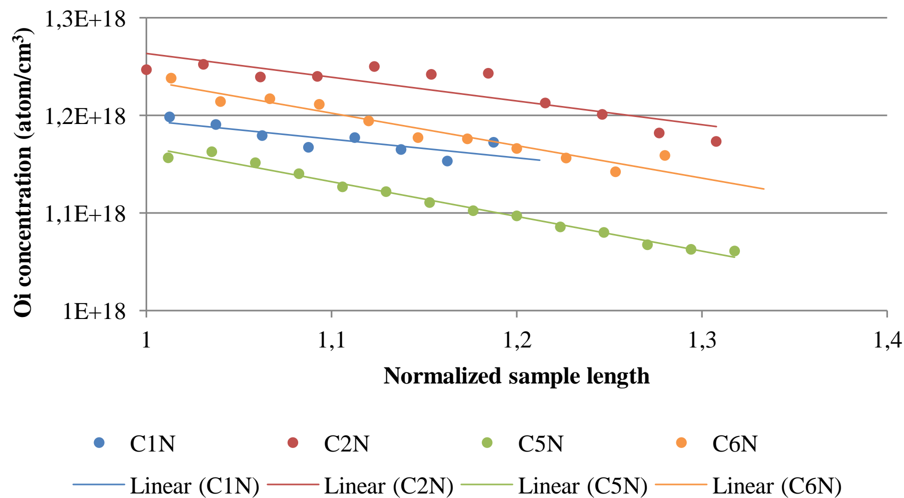

Figure 48 - Interstitial oxygen measurements along the first line (ingot center) of the early body as a function of the sample length, for all samples in as-grownconditons.

In Figures 49 and 50, interstitial oxygen and resistivity measurements as a function of the sample radius are shown for C2N and C5N, respectively. Here, the focus remains on the curves deflection of, which is more significant in the crown region due to growth process instabilities.

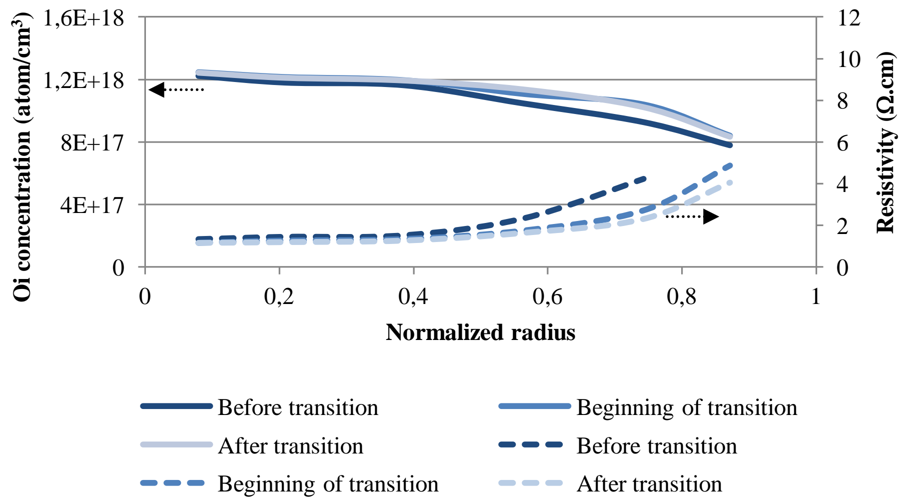

Figure 49 - Interstitial oxygen and resistivity measurements as a function of the sample radius for C2N in as-grown conditions.

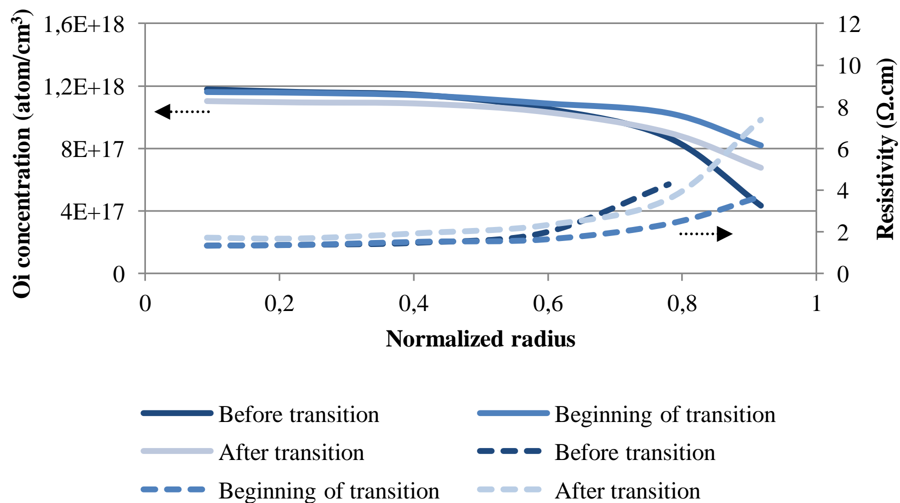

Figure 50 - Interstitial oxygen and resistivity measurements as a function of the sample radius for C5N in as-grown conditions.

7.5. Thermal donors (TDs) dissolution

In Figure 51, interstitial oxygen measurements along the first vertical line as a function of the sample length for all samples after TDs annihilation, is shown. The difference between oxygen concentration before and after TD annealing is small and not so easily observable. In Figure 52, the same is illustrated but only for the early body region, where a small increase in interstitial oxygen concentration for all samples as a result of TD dissolution is shown.

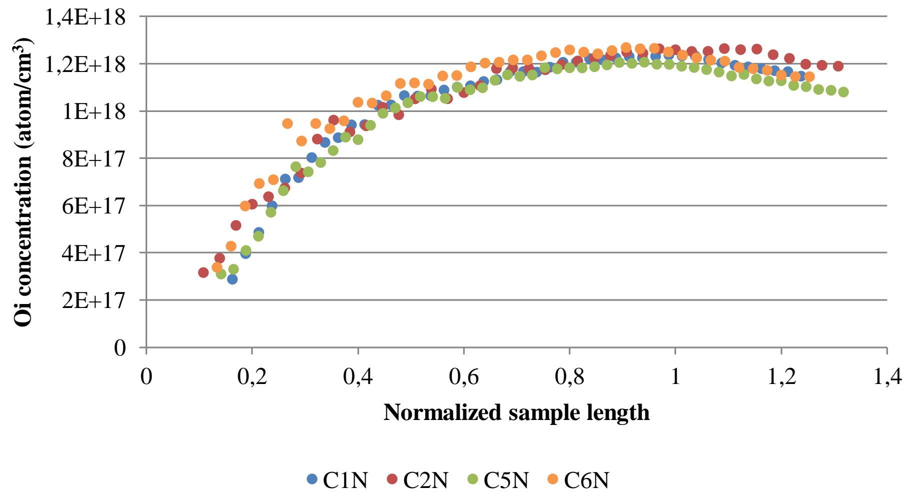

Figure 51 - Interstitial oxygen measurements along the first vertical line (ingot center) as a function of the sample length, for all samples after TDs annihilation.

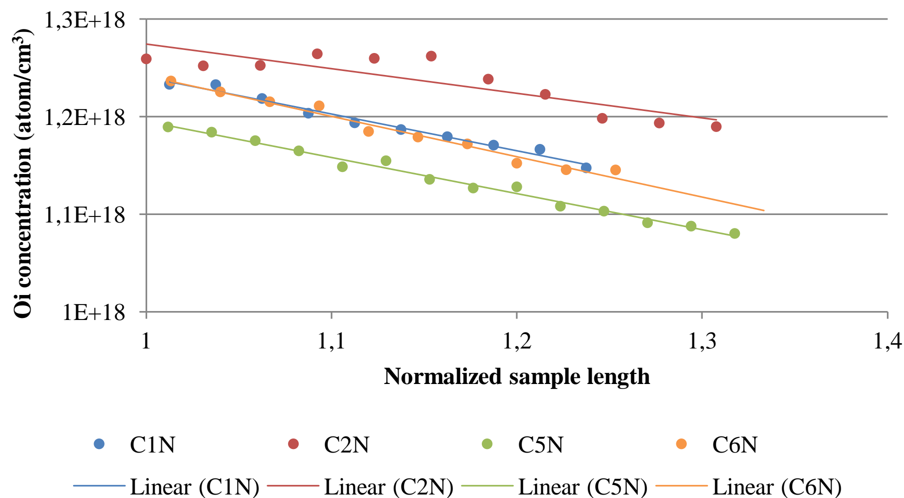

Figure 52 - Interstitial oxygen measurements along the first line (ingot center) of the early body as a function of the sample length, for all samples after TD annealing.

Figures 53 and 54 illustrate resistivity measurements along the first vertical line as a function of the sample length, for all samples before and after TD annealing, respectively. In Figure 53, resistivity decreases along the sample length. In this case, the resistivity is determined by dopant and TD concentration. In Figure 54, resistivity remains constant along the sample length, since it is determined only by the dopant concentration.

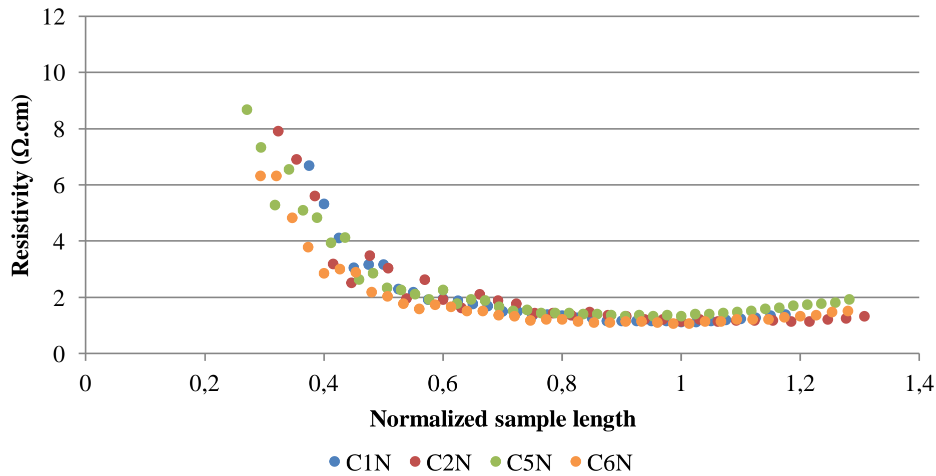

Figure 53 - Resistivity measurements along the first vertical line (ingot center) as a function of the sample length, for all samples before TDs annihilation.

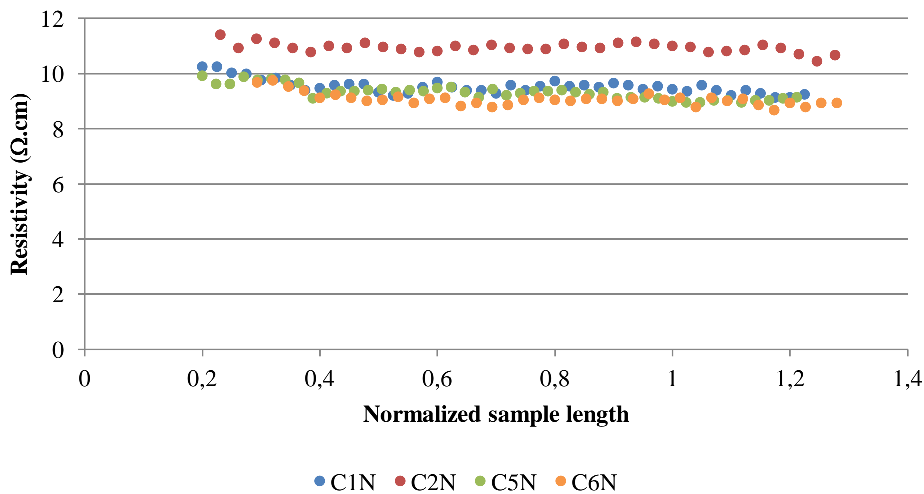

Figure 54 - Resistivity measurements along the first vertical line (ingot center) as a function of the sample length, for all samples after TDs annihilation.

In Figure 55, the resistivity difference between before and after TDs annihilation for all samples along the first vertical line as a function of the sample length is illustrated. The resistivity variation can represent TD distribution.

In Figure 56, the average difference in resistivity between before and after TD annealing for the whole samples area is illustrated. The sample C2N reveals the higher resistivity variation and the sample C5N shows the lower. The samples C1N and C6N show similar values.

In Figure 57, lifetime measurements with PL imaging of the samples C2N and C5N after TD annealing are represented. After transition, C5N still shows a higher lifetime.

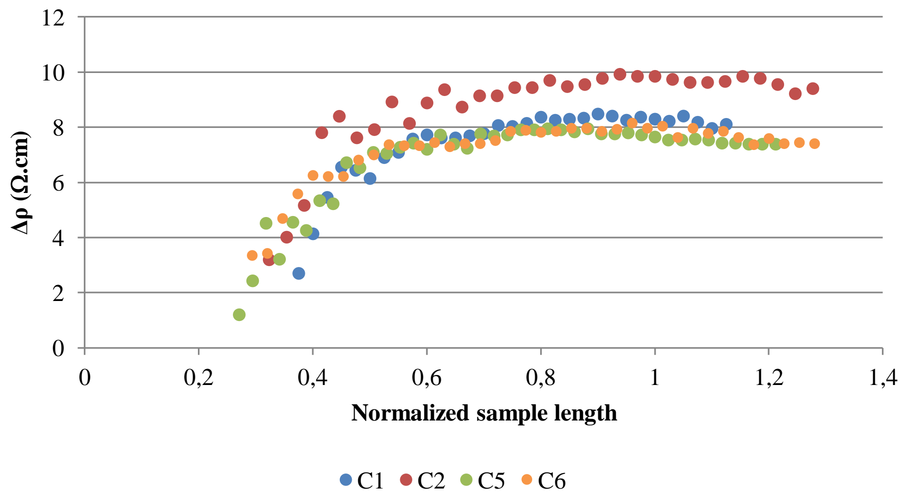

Figure 55 – Resistivity difference between before and after TDs annihilation for all samples along the first vertical line (ingot center) as a function of the sample length.

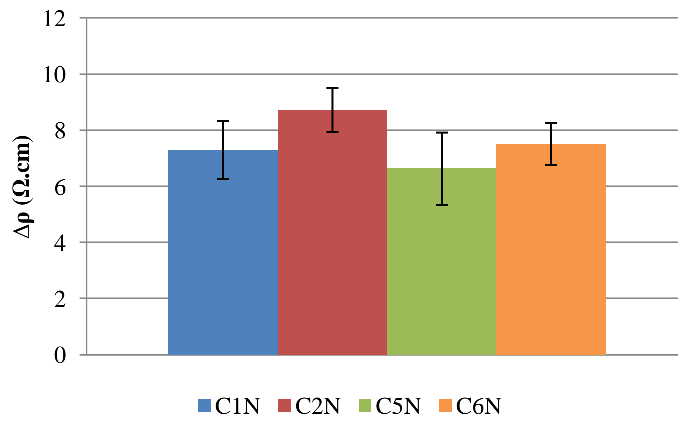

Figure 56 - Average difference in resistivity between before and after TDs annihilation for the whole samples area.

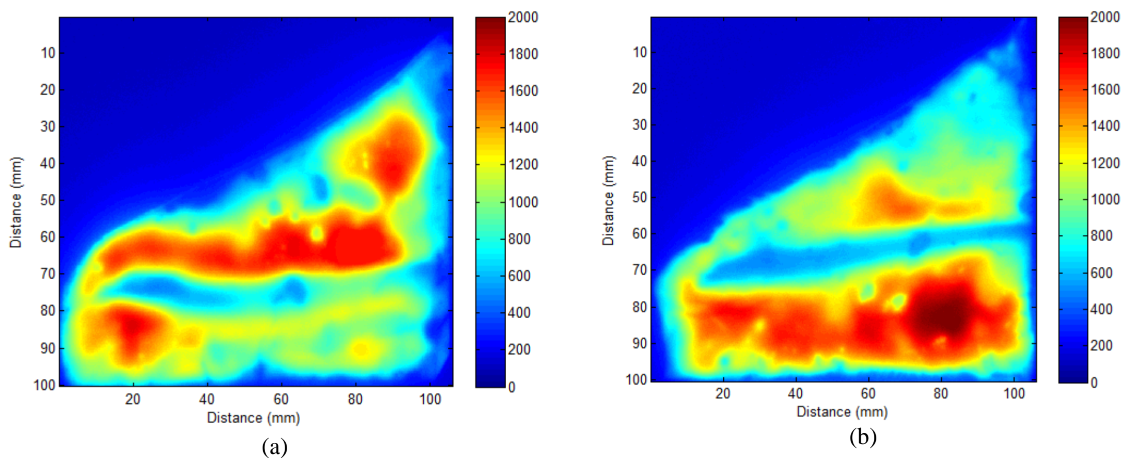

Figure 57 - Lifetime (µs) measurements with PL imaging of the sample (a) C2N and (b) C5N, after TD annealing.

7.6. Comparison between n- and p-type materials

In Figure 58, the sample radius as a function of length for C2N and C2P is illustrated. The sample shape and also growing conditions are similar; then a comparison between both is possible to establish.

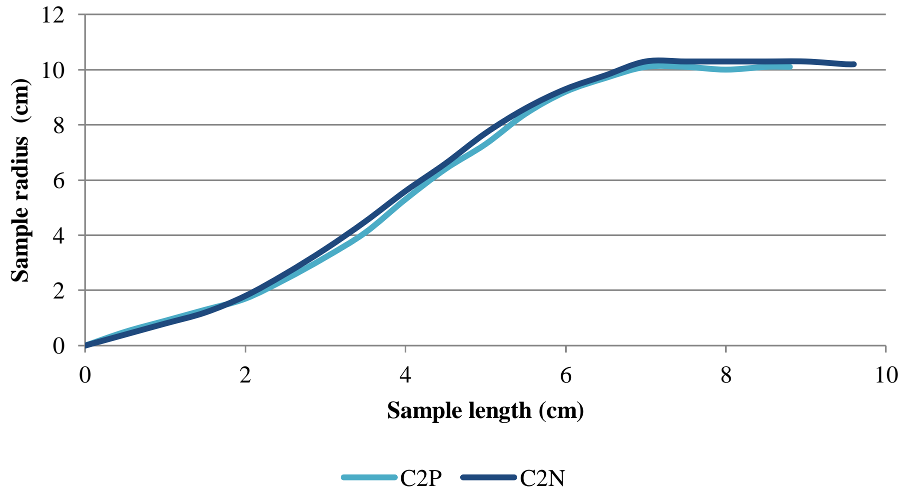

Figure 58 - Sample radius as a function of length for C2N and C2P.

7.6.1. Oxygen and resistivity measurements in as-grown conditions

Figures 59, 60 and 61 show the FPD density along the first, third and sixth vertical lines as a function of sample length for both samples C2P and C2N. In Figure 59, the respective P-band is also represented. In Figure 59, the FPD density for C2P seems to be lower than that for C2N. In Figure 60, similar FPD density curves are shown but with a small shift. In Figure 61, FPD density for C2P shows to be lower than that for C2N once again. It is also noted that the samples do not have the same length.

Figure 62 shows the interstitial oxygen measurements along the first line for both samples C2N and C2P before TDs annihilation. The oxygen concentration is just slightly different in the beginning due to the presence of striations which are related to an unstable melt.

Figure 63 illustrates both resistivity and interstitial oxygen measurements along the first line for sample C2N before TDs annihilation. The sample C2N starts with a higher resistivity and then it decreases as a function of sample length. Figure 64 shows the same information but in relation to the sample C2P. The sample C2P starts with a lower resistivity and increases with the sample length.

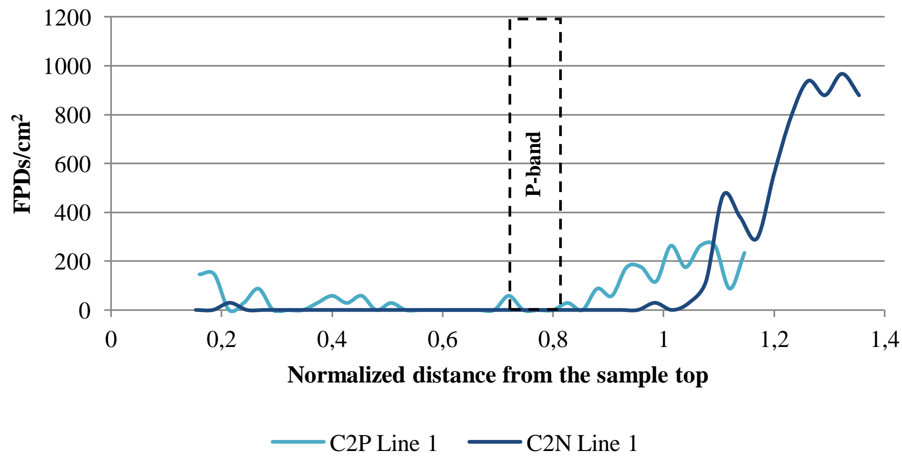

Figure 59 - FPD density along the first line measured (ingot center) as a function of sample length of samples C2P and C2N, with 2 mm of resolution. The respective P-band position is also represented.

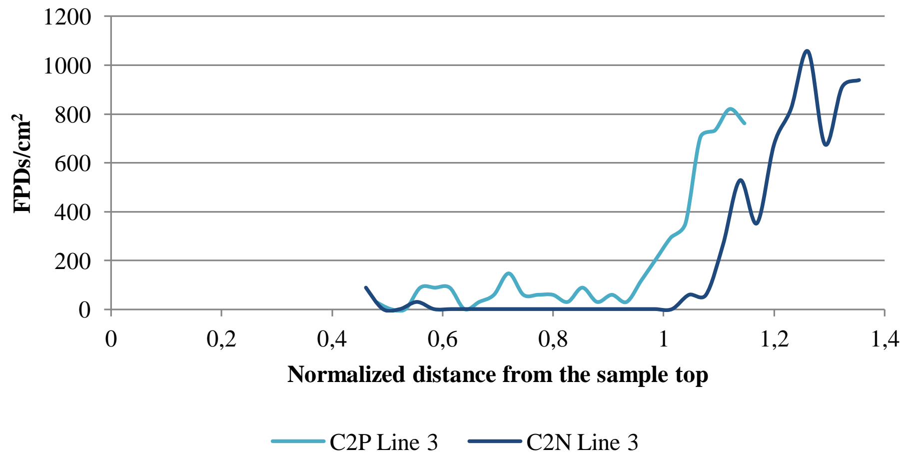

Figure 60 - FPD density along the third line measured as a function of sample length of samples C2P and C2N, with 2 mm of resolution.

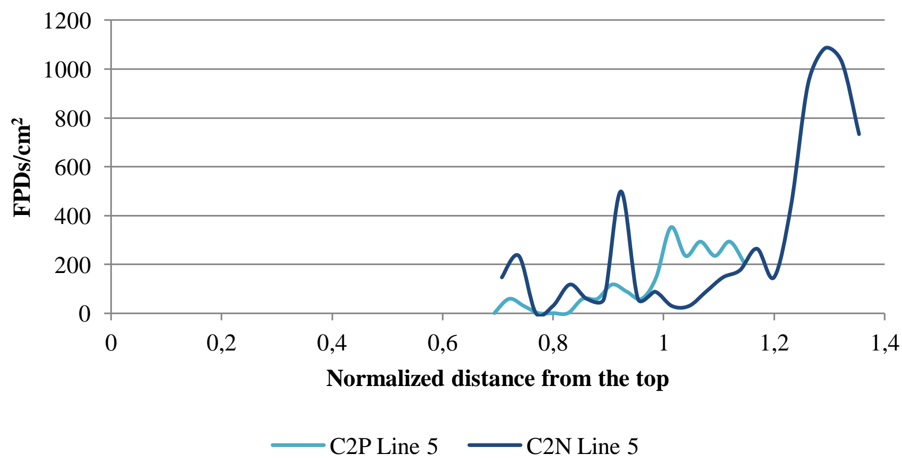

Figure 61 - FPD density along the fifth line measured as a function of sample length of samples C2P and C2N, with 2 mm of resolution.

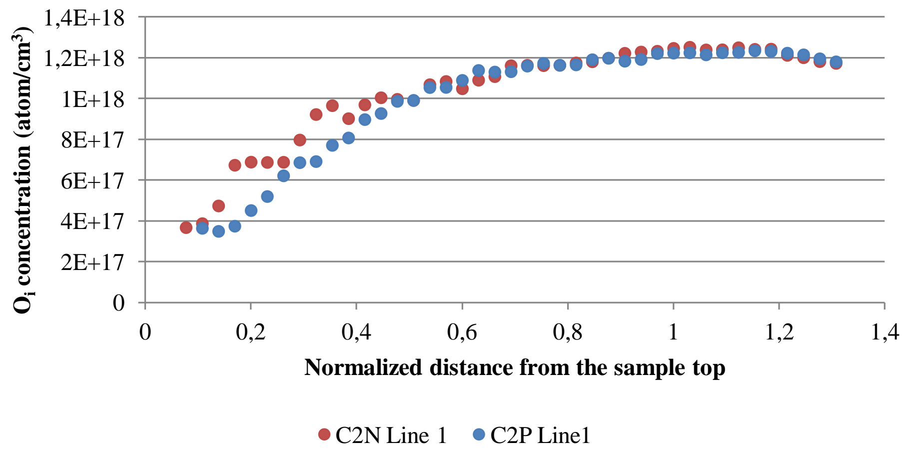

Figure 62 - Interstitial oxygen measurements along the first line (ingot center) for both samples C2N and C2P., before TDs annihilation.

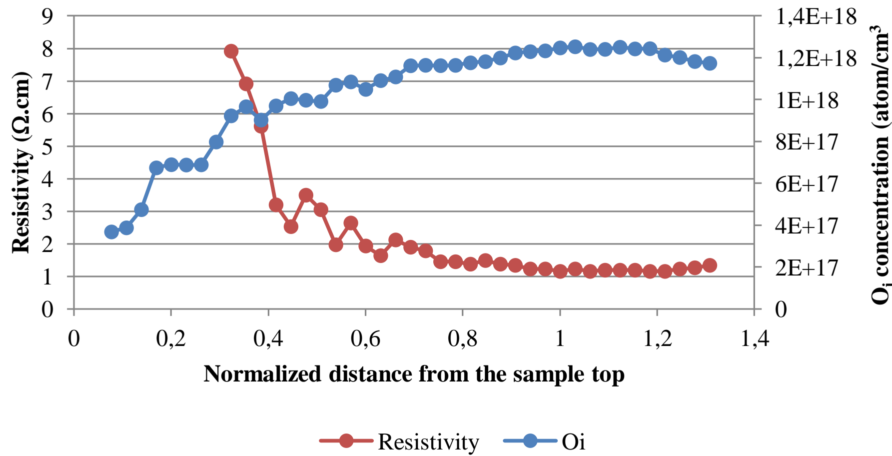

Figure 63 - Resistivity and interstitial oxygen measurements along the first line (ingot center) for sample C2N, before TDs annihilation.

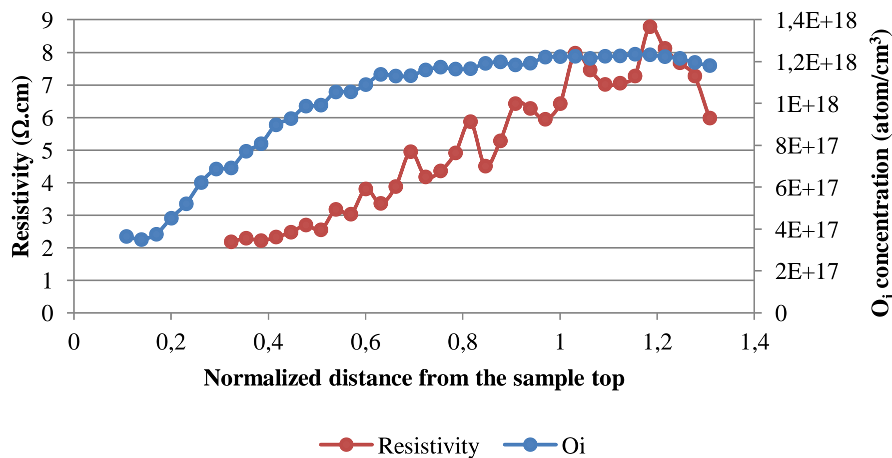

Figure 64 - Resistivity and interstitial oxygen measurements along the first line (ingot center) for sample C2P, before TDs annihilation.

7.6.2. Thermal donors (TD) dissolution

In Figure 65, both resistivity and interstitial oxygen measurements along the first line for sample C2N after TDs annihilation are illustrated. After TDs dissolution, the final resistivity is determined by dopant concentration alone. The sample C2N has the lower dopant concentration (see Figure 67) and the higher resistivity. In Figure 66, the same information is given but for the sample C2P. The sample C2P has a higher dopant concentration and the lower resistivity.

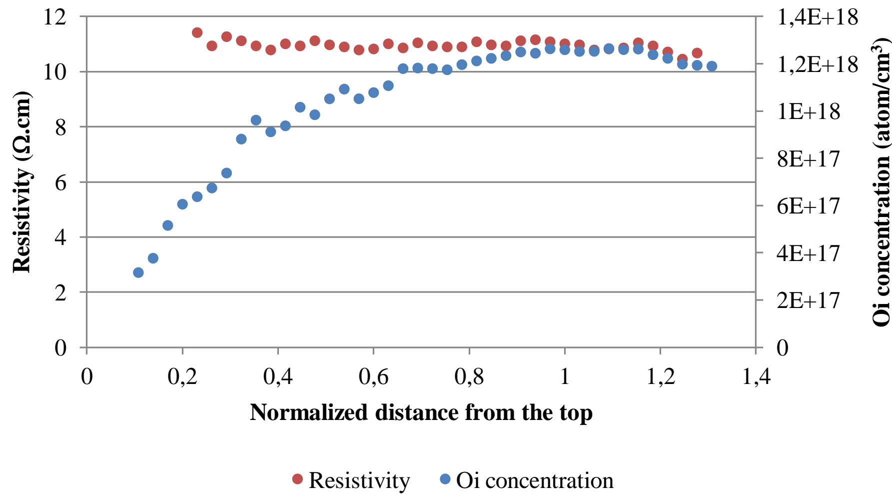

Figure 65 - Resistivity and interstitial oxygen measurements along the first line (ingot center) for sample C2N, after TDs annihilation.

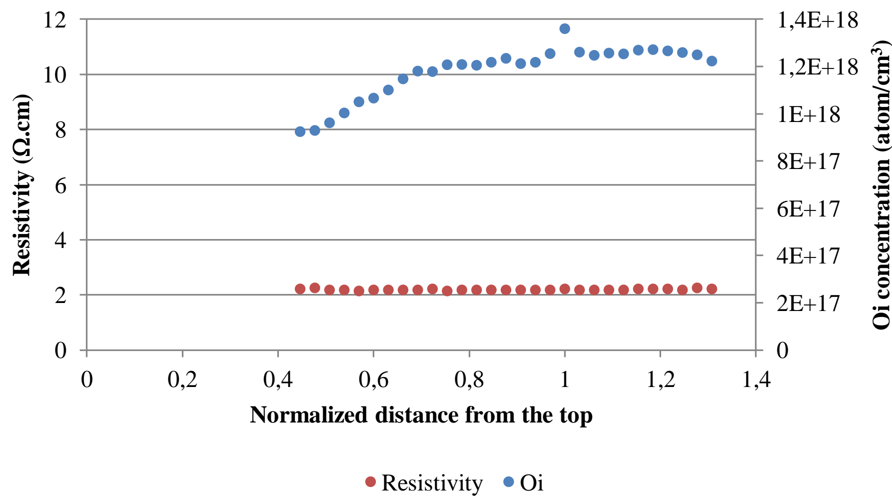

Figure 66 - Resistivity and interstitial oxygen measurements along the first line (ingot center) for sample C2P, after TDs annihilation.

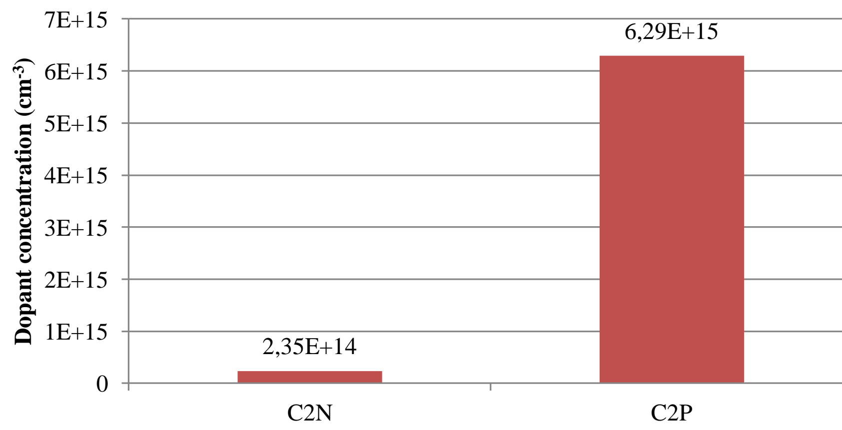

Figure 67 - Dopant concentration for the average resistivity for the whole samples area, after TDs annihilation.

8. Discussion

The FPD are delineated by using Secco etching and can be easily recognized under light microscope by the wedge-shaped etch pattern. Etch pits without flow patterns are also observed and they are not related to D-defects but to crystallographic defects. Therefore, the FPD density calculation just takes into account the presence of the wedge-shaped etch pattern, as well the presence of D-defects, as illustrated in Figure 38.

A light microscope sensibility test was performed for the first vertical line with 50x and 100x of magnification to determine which resolution would be better suited for further measurements. These observations were carried out for samples C5N and C6N and the final conclusion is the same. As illustrated in both Figures 39 and 40, it is possible to verify a similar FPD distribution trend. However, a significant variation in its density is evident between different magnifications. Two possible reasons are related to the manual sample movement and non-intentional plate movements. When this happens, a significant error is introduced during the defect counting since some defects can be counted twice, as illustrated in Figure 41. Furthermore, the FPD density that was measured using 100x magnification were more unstable compared to the measurements that were made using 50x magnification. For this reason, 50x magnification was chosen for further measurements. The calculation method consists of counting the D-defects of each picture which is then divided for the picture area.

The normalization was performed in relation to the shoulder since all samples were not grown and cut with the same length. Still, all samples have at least 20 mm of length after the shoulder.

According to Voronkov's theory, the dominant microdefect type of the grown CZ silicon crystal is vacancy defects or interstitial oxygen. Their formation is determined by the V/G ratio, where *V* is the growth rate and *G* is the axial temperature gradient near the solid-liquid interface of the crystal.

For *V/G* above the critical value, vacancies are incorporated. During the cooling, these microdefects tend to agglomerate, forming larger voids. When V/G is slightly larger than the critical ratio (thus low vacancy concentration), extended defects, such as vacancy-oxygen and oxygen precipitates, are produced instead of vacancy agglomeration. For this reason, the main vacancy-containing region of a crystal, i.e., where voids are generated, is surrounded with a narrow marginal band containing oxide particles, the P-band.

These voids, formed by agglomerates of vacancies, have the designation of FPD if they are characterized by light microscope, which is the case. The FPD density was determined for all samples. Figure 42 shows the FPD density for samples C2N and C5N. Figure 43 shows the FPD density for samples C1N and C6N. P-band for each sample is also illustrated. Samples were grouped for the purpose of future comparisons.

Defect regions, such as I-region and V-region, can be defined since it was found that the defect density was different in different areas. Lower FPD density can be found in the interstitial region when compared to the vacancy region, as predicted by Voronkov's theory. Still, vacancies can be found in I-region due to fluctuations on interface.

In Figure 42, C5N shows a higher FPD density in V-region compared to C2N. In fact, C5N has a longer transition area (see Table 3) when compared to C2N. A longer transition time indicates a lower cooling rate at the crystal-melt interface. Longer growing time leads to a longer time for the vacancies agglomerate. On the other hand, C2N took less time to form the transition area (Table 3), which also means that a higher cooling rate was achieved. As a result, vacancy agglomeration rate is lower and, consequently, the FPD density is also lower. Nevertheless, a higher drop on FPD density is observed for C5N in the beginning of the early body.

Concerning C1N and C6N (Figure 43), the latter has the longest transition time, hence the lowest cooling rate which leads to a longer time to form voids. C1N starts to have higher FPD density in the

V-region but then the sample C6N reaches a higher peak followed also by a higher drop in the beginning of the early body.

The most compelling evidence is the relation between transition time (shoulder growing time) with the formation of voids in V-region and its density in the early body region. Longer transition times are associated with a lower cooling rate and higher void density followed by its decrease on early body region. Furthermore, the crown tapered angle also affects the FPD density. The results show that C5N has a higher crown tapered angle compared to C2N and the FPD density curve starts earlier than that for C2N. On the other hand, C1N and C6N have similar crown tapered angle and both density curves starts approximately at the same position.

Equally relevant, looking to the I-region, FPD density oscillations are visible and are larger for C6N then C5N, C1N and C2N. Ignoring the sample C6N, the sample order above corresponds also to the lifetime sequence, i.e., C5N as the higher lifetime and C2N the lower lifetime. C1N represents the middle situation. The sample C6N has more density oscillations due to growth process fluctuations which are not discussed in this work. It is clear that the crystal growth process as a significant influence on the material quality from the start.

Light microscope pictures from different regions, before and after transition, are illustrated in Figures 44 and 45, respectively. In general, before transition no defects are found or they density is too low. After transition, FPD density is different for each sample. Comparing C2N with C5N, it was found that the FPD density was lower C2N. The FPD densities were 557 FPD/cm^2 and 704 FPD/cm^2, respectively. Also, comparing C1N with C6N, for a similar sample length, the FPD density is coincidently similar, around 733 FPD/cm^2, but that does not happened for all V-region for the reasons already mentioned before.

The P-band starts when the pull speed is quickly raised, where the transition area begins, and ends where transition also ends. Since thermal gradient increases with the distance from the ingot center to the edge, V/G ratio decreases as a function of ingot radius and the P-band as a deflected shape. The P-band can be visualized in Figures 42 and 43. The P-band position was based on PL images (Figure 32) as a very narrow dark blue region in the sample center which indicates the region with lower lifetime.

The incorporation of oxygen in the melt results from the gradual dissolution of the silica crucible walls. Since SiO is very volatile, most of the oxygen evaporates from the melt surface, but a small part remains in the melt which is then incorporated into the silicon crystal through the crystal-melt interface.

Lin and Benson [27] recognized that the relationship between oxygen concentration and available melt surface is not linear. The oxygen evaporation and, consequently, the oxygen concentration in the crystal, depend on the sample diameter variation. When the crystal reaches the desirable diameter and the melt is almost covered, the evaporation seems to remain nearly constant and the oxygen concentration in the crystal is linear along the fraction solidified.

In Figure 46, interstitial oxygen measurements along six vertical lines as a function of the sample length are illustrated for the four main samples characterized. Note that the horizontal axis represents the normalized sample length in relation to the shoulder starting point. In this Figure, the oxygen concentration decreases from the ingot center towards the edge, where line 1 represents the closest line to the center and line 6 the closest line to the edge. There are some differences concerning to the oxygen distribution, especially when its maximum concentration is achieved. For all situations, this maximum concentration is obtained when the sample diameter is also at its maximum. However, this maximum concentration point is not the same for all ingots. In fact, the crown tapered angle has a clear influence in this matter. Comparing C2N with C5N, the maximum concentration point for the first one is located quite after the transition started. On the other hand, C5N shows a maximum concentration point before the transition begins. Another key point lies in the fact that the maximum concentration point for C1N and C6N are similar, and as have already been mentioned, these ingots have similar crown tapered angles. For this reason, it is possible to say that this maximum

concentration point of interstitial oxygen is influenced by the crown shape, moving up (neck direction) with the crown tapered angle decreasing, and moving down with the crown tapered angle increasing.

In Figure 47, interstitial oxygen measurements along the first line as a function of the sample length are illustrated for the four main samples. The interstitial oxygen distribution increase along this part of ingot until it reaches a maximum point followed by its discrete decreasing. In the crown region, C2N has higher oxygen concentration compared to C5N. Concerning to C1N and C6N, these are always a middle situation. After transition, the same situation is observed. In Figure 48, the same information is given, but the focus remains on the crystal region after transition, the early body. If the growth conditions are kept similar among ingots, it is possible to predict the final crystal quality. In the early body region, C2N has de higher oxygen concentration and its decreasing rate is lower than that for C5N and C6N. This means that its crystal body is likely to have a higher oxygen concentration compared to the other ones. In contrast, the ingot C5N shows the lower oxygen concentration in this region and its decreasing rate is also higher, which means that this ingot will probably have a higher quality when compared to the other ingots.

In Figures 49 and 50, interstitial oxygen and resistivity measurements as a function of the sample radius are shown for C2N and C5N, respectively. Here, the important aspect is the deflection of the curves. Since G often increases significantly from the crystal-melt interface center to the periphery, the radial cross section of the crystal shows a distinct deflection of D-defect distribution. This deflection is more significant before transition, i.e, crown region, since the crystal growth process is very instable in that part even with low crystallization rates. This situation is similar for the other ingots, C1N and C6N.

Given these points, a strong connection between the crown tapered angle and oxygen concentration and distribution can be established. For a higher crown tapered angle, longer is the growing time (lower the cooling rate) and higher the oxygen evaporation. The maximum concentration point is also reached before the transition starts, which can be consequently related to the P-band position. Having lower oxygen concentration in the early body may indicate a lower oxygen concentration in the crystal body.

Interstitial oxygen is electrically inactive in the form that is incorporated, thus it does not have influence on the lifetime. Though, depending on the thermal history during the crystal cooling, different stages of oxygen agglomeration can be observed: thermal donors (TDs). For this reason, interstitial oxygen incorporation is an important factor during all crystal growth process.

Upon temperatures around 450ºC, electrically active oxygen agglomerates are generated from the presence of interstitial oxygen. All the silicon crystals experience this temperature range during the cooling process from the melt temperature to room temperature, when oxygen becomes supersaturated and may precipitate. Fortunately, TDs can be eliminated by a heat treatment around 800ºC. For this reason, all samples were subject to an annealing treatment around this temperature for 10s, which is enough to dissolve TDs [88]. It is known that carbon is another important impurity incorporated into the melt during the crystal growth process which has influence on thermal donor generation and on oxygen precipitation. However, its concentration is always bellow 0.5 ppma which has not significant influence.

A rapid thermal process (RTP) oven was used for this purpose. First, a cleaning step was performed, since it is necessary to have a very clean environment inside the oven, free of contaminants from early experiments. The cleaning steps are shown in Table 5. After the cleaning step, the sample is introduced inside the oven. The TD annealing steps are shown in Table 6.

In Figure 51, interstitial oxygen measurements along the first vertical line as a function of the sample length for all samples, after TD annealing, are illustrated. The difference between oxygen concentration before and after TD annealing is small and not so easily observable. Despite small differences on interstitial oxygen concentration, significant differences on TD formation are verified, since their concentration has a linear relationship with interstitial oxygen concentration, being proportional to the fourth power of the latter [34]. In Figure 52, the same information is given only for

the early body length. Similarities with Figure 47 are shown. As a matter of fact, it is possible to verify the small increase in interstitial oxygen concentration for all samples as a result of TD dissolution. Once again, C2N has the higher oxygen concentration and its decreasing rate is also the lower one. Under those circumstances, its crystal body will have a higher oxygen concentration compared to the other ones, as mentioned before. On the contrary, the ingot C5N shows again the lower oxygen concentration in this region and its crystal body probably will have higher quality.

Since TDs are electrically active, they will have also an influence on material resistivity. Figures 53 and 54 illustrate resistivity measurements along the first vertical line as a function of the sample length, for all samples before and after TD annealing, respectively. Also, in Figure 55, the resistivity difference between before and after TD annealing is represented, which can also represent its distribution. Before TD annealing, resistivity decreases along the sample length, whereas after TD annealing, resistivity remains constant along the sample length. Since the incorporation of interstitial oxygen in the growing crystal will change according to diameter variations, these results are according to the expected. It is clear that TDs concentration and distribution has a strong influence of on the material, especially for C2N which has the higher resistivity variation. The sample C2N has the higher cooling rate which means an higher oxygen incorporation during the process. Note that, after TDs dissolution, the final resistivity is determined only by dopant concentration alone.

In Figure 56, the average difference in resistivity between before and after TD annealing for the whole samples area is illustrated. The sample C2N reveals the higher resistivity variation between before and after TDs dissolution. In contrast, the sample C5N shows the lower resistivity variation. The samples C1N and C6N show similar outcomes and represent the middle situation when compared to the other two. These results are according to what was discussed before.

In Figure 57, lifetime measurements with PL imaging of the samples C2N and C5N after TD annealing are illustrated. It is interesting how opposite the pictures are in terms of color, i.e., in terms of lifetime distribution. Before transition, C5N reveals a higher lifetime than that for C2N. Still, after transition, C5N shows a higher lifetime and, consequently, higher material quality. Actually, the lifetime after TD annihilation for C2N was not the expected since that should be similar to C5N on V-region. Thus, lifetime is influenced not just by the presence of TD but also by other oxygen precipitates which were formed during its thermal history due to the cooling rate.

It is known that the crown region is not of interest for semiconductor material industry. For this reason, a higher quality is expected and desired on early body and subsequent crystal body. Still, if we understand the role of oxygen in the crown region, it will be possible to control it and possibly reduce the area of the early body, thus reduce the amount of material that is discharged before wafering. Under those circumstances, ingot growth conditions of C5N would be chosen over the other three.

The formation of microdefects in CZ silicon crystals is affected by the presence of acceptor and donor impurities. In this work, also a comparison between n- and p-type materials was made. In Figure 58, the sample radius as a function of length for C2N and C2P is illustrated. The sample shape and also growing conditions are similar; therefore a comparison between both is possible to proceed with.

Figures 59, 60 and 61 give the FPD density along the first, third and sixth vertical lines as a function of sample length for both samples C2P and C2N. In Figure 59, the respective P-band is also shown. For the first and fifth lines measured, FPD density for C2P seems lower than that for C2N. However, the same does not happen for the third line measured, when similar FPD density curves are shown but with a small shift.

It is known that concentration of voids decrease in p-type, and increase in n-type, when dopant concentration is higher than about 1×10^{19} atoms/cm^3 (see Figure 68) [90]. However, the dopant concentrations that were found are about 2.35×10^{14}atoms/cm^3 for C2N and 6.29×10^{15}atoms/cm^3 for C2P [91]. Both are significantly below that limit, therefore voids concentration should be similar as it is for the third line measured. In the first line measured, the sample C2N has more length of early body than C2P and the last FPD density points for C2P shows a trend to increase. So probably, the FPD density curve for C2P reaches similar values to C2N. The same happens for the fifth line measured.

In Figure 62, interstitial oxygen measurements along the first line for both samples C2N and C2P, before TD annealing, is illustrated. The oxygen concentration is slightly different in the beginning due to the presence of striations which are related to an unstable melt. However, both curves are supposed to be similar and they actually are from some point, when the growth process is more stable.

In Figures 63 and 64, resistivity and interstitial oxygen measurements along the first line for sample C2N and C2P, respectively, in as-grown conditions are illustrated. In contrast to interstitial oxygen concentration curves, resistivity curves have different behavior when both are compared. The sample C2N starts with a higher resistivity and then it decreases as a function of sample length due to the increase of TDs. On the contrary, the sample C2P starts with a lower resistivity and increases with the sample length. This situation can be related to how and when the dopant is added during the crystal growth process. This situation can be related to the dopant volatility. For instance, phosphorus is a very volatile compound, most of it evaporates due to the high temperature of the melt. On the other hand, boron is distributed according to its segregation coefficient

In Figures 65 and 66, resistivity and interstitial oxygen measurements along the first line for samples C2N and C2P, after TD annealing, are illustrated. After TDs dissolution, the final resistivity is determined by dopant concentration alone, and it is shown that C2P has a higher concentration (see also Figure 67).

9. Conclusions

The lifetime variations between different samples and the relationship between lifetime and the total area, where the crown tapered angle play a key role, were observed. The crown with the higher tapered angle has shown the higher lifetime while the lower crown tapered angle has the lower lifetime. Thus, the motivation of this work was to understand the role of oxygen on high defects density regions and its influence on lifetime.

All samples were characterized in terms of lifetime, resistivity, interstitial oxygen and TD concentration and distribution. FPD density was determined and the defects nature evaluated by light microscope observations. Samples passivation and lifetime measurements were performed at IFE.

A strong correlation between the crown tapered angle and oxygen concentration and distribution was established. Higher crown tapered angle corresponds to longer growing time (lower cooling rate) and higher oxygen evaporation. Since the melt temperature is higher in the beginning of the crystal growth, as well as the free melt surface area, the oxygen evaporation will be higher. Also a higher void density is achieved after the transition (shouldering stage) followed by its decrease in the early body region. Lower oxygen concentration in the early body can also indicate a lower oxygen concentration in the crystal body, if the crystal growth conditions are kept similar. In fact, when increasing the growth rate, the crystal diameter decreases, the free melt surface area increases and, consequently, the oxygen evaporation increases. Therefore, the quality of the top ingot significantly depends on the free melt surface area, on the oxygen dissolution from the crucible and on the heater temperature.

Interstitial oxygen is an important factor during all crystal growth process not due to the form as it is incorporated into the crystal, but due to the different stages of oxygen agglomeration which can be observed, especially thermal donors (TDs) upon temperatures around 450ºC. As expected, the resistivity of the samples investigated decreases as a function of sample length and, after TD annealing, it remains constant. The ingot with the lower crown tapered angle reveals the higher resistivity variation. In this case, the dopant concentration seems be dependent on the cooling rate, which shows to be the highest. In contrast, the ingot with higher crown tapered angle and consequent lower cooling rate reveals the lowest resistivity variation.

In conclusion, the early crystal body quality can be influenced by the top ingot quality depending on the interstitial oxygen concentration and distribution. The crystal body was not the object of this study, however, analyzing the early body from each ingot, some connection between the material lifetime and the crystal growth process can be established.

10. Further work

In the future, it would be interesting to proceed with the same characterization process for the whole ingots body in order to verify if it is possible to predict the crystal body quality from the early body quality. This is only possible if the body growth conditions correspond to that of the crowns which were studied on this thesis work.

This work would be focused on three regions of crystal body, i.e., on the early body, on the middle of the crystal body and near the tail. Preparation of samples from each region is required to perform interstitial oxygen and resistivity measurements before and after TD annihilation, using FTIR and four-point probe, respectively. Lifetime measurements are also necessary and can be obtained by using PL imaging. Defects nature and distribution can also be determined by using light microscope and SEM, if a more detailed analysis is required. Samples oxidation may also be important to perform in order to verify oxygen precipitates and stacking faults distribution. SEM pictures from specific sample regions after oxidation could also be something interesting to analyze.

More correlations between the results of this thesis with the process parameters of the investigated ingots would be important and this is the topic of a PhD study. Furthermore, it would be interesting and useful to couple all these experimental results with numerical models in order to verify if it is possible to predict the final material quality.

11. References

[1] Stubhaug, E., Ekker R., 2005. Temperature and injection dependent lifetime spectroscopy, Norwegian University of Science and Technology, Faculty of Natural Sciences and Technology, Department of Physics, Trondheim, Norway.

[2] Khanna, V., 2005. Physical understanding and technological control of carrier lifetimes in semiconductor materials and devices: A critique of conceptual development, state of the art and applications, Solid State Devices Division, Central Electronics Engineering Research Institute, Rajasthan, India.

[3] Zeghbroek, B. Van, 2011. Principles of Semiconductor Devices (available online in http://ecee.colorado.edu/~bart/book/contents.htm, accessed in September 2013).

[4] http://cnx.org/content/m43554/latest/

[5] Goetzberger, A., Knobloch, J., Voss, B., 1998. Crystalline Silicon Solar Cells, John Wiley & Sons, England.

[6] Gupta, D. C., Bacher, F. R., Hughes, W. M., 1998. Recombination Lifetime Measurements in Silicon, American Society for testing and materials, West Conshohocken.

[7] Li, Sheng S., 2006. Semiconductor Physical Electronics. Department of Electrical and Computer Engineering, Second Edition, University of Florida, USA.

[8] Macdonald, D., 2001. Recombination and Trapping in Multicrystalline Silicon Solar Cells, PhD Thesis, Australian National University.

[9] http://www.iue.tuwien.ac.at/phd/entner/node14.html

[10] Czochralski, J., 1928. *Ein neus verfahren zur messung des kristallisationsgeschwindigkeit der metalle*, Z. Phys. Chem. 92, 219.

[11] Teal, G. K., Little, J. B., 1955. Method of producing semiconductive bodies, US Patent No. 2,683,676.

[12] Theurer, H. C., 1962. Method of processing semiconductive materials, U.S. Patent No. 3,060,12.

[13] http://ywang13.myweb.usf.edu/make.jpg

[14] Válek, L., Šik, J., n/d. Defect Engineering During Czochralski Crystal Growth and Silicon Wafer Manufacturing, Czech Republic.

[15] Newman, R. C., 1982. Defects in Silicon, Rep. Prog. Phys., Vol. 45.

[16] Shimura, F., 1994. Oxygen in Silicon, Academic Press, Inc, San Diego.

[17] Luque, A., Hegedus, S., 2011. Handbook of Photovoltaic Science and Engineering, Second Edition, John Wiley & Sons.

[18] http://meroli.web.cern.ch/meroli/Lecture_silicon_floatzone_czochralski.html

[19] http://www.pvatepla.com/en/products/crystal-growing-systems/pva/czochralski-process/overview

[20] Dash, W. C., 1958. The growth of silicon crystals free from dislocation, eds. R. H. Doremus, B. W. Roberts and D. Turnbull, pp. 361-85, New York.

[21] O'Mara, W. C., Herring, R. B., Hunt, L. P., 1990. Handbook of Semiconductor Silicon Technology, Noyes Publications.

[22] Winkler, J., Neubert, M., Rudolph, J., 2010. Nonlinear model-based control of the Czochralski process I: Motivation, modeling and feedback controller design, Journal of Crystal Growth, Volume 312, Issue 7, pages 1005-1018.

[23] Davis et al, 1980. Impurities in silicon solar cells, IEEE Transactions on Electron Devices, vol. ED-27, pages 677-687.

[24] Chaney, R. E., Varker, C. J., 1976. The dissolution of fused silica in molten silicon, J. Cryst. Growth 33, 188-190.

[25] Kaiser, W., Keck, P. H., 1957. J. Appl. Phys. 38.

[26] Möller, H. J., 1993. Semiconductors for Solar Cells, Artech House, Inc.

[27] Lin, W., Benson, K. E., 1987. Annual Review of Materials Science, 17, 273.

[28] Lidroos, V., Tilli, M., Lehto, A., Motooka, T., 2010. Handbook of silicon based mems materials and technologies, Micro & Nano Tecnhologies Series, Elsevier, Oxford, UK.

[29] Nishi, Y., Doering, R., 2008. Handbook of Semiconductor Manufacturing Technology, Second Edition, CRC Press, Taylor and Francis Group, USA.

[30] Gilles, D., Weber, E. R., Hahn, S., 1990. Phys. Rev. Lett. 64, 196.

[31] Myers, S. M., Seibt, M., Schröter, W., 2000. J. Appl. Phys. 88, 3795.

[32] Fuller, C. S., Ditzenberger, J. A., Hannay, N. D., Buehler, E., 1954. Phys. Rev. 96, 833.

[33] Kaiser, W., Frisch, H. L., Reiss, H., 1958. Phys. Rev. 112, 1546.

[34] Claybourn, M., Newman, R. C., 1988. Thermal donor formation and the loss of oxygen from solution in silicon heated at 450 °C, Applied Physics Letters, 52(25): p. 2139-2141.
[35] Bruzzi, M., Menichelli, D., Scaringella, M., 2006. J. Appl. Phys 99, 093706.
[36] Hu, Y., Schøn, H., Øvrelid, E. J., Nielsen, Ø., Arneberg, L., 2012. Investigation thermal donors in n-type Cz silicon with carrier density imaging, AIP Advances 2, 032169.
[37] Liaw, H. M., Varker, C. J., 1977. Semiconductor Silicon, edited by H. R. Huff and E. Sirtl Vol. 2, p. 116, The Electrochemical Society.
[38] Kanamori, A., Kanamori, M., 1979. J. Appl. Phys. 50, 8095.
[39] Cazcarra, V., Zunino, P., 1980. J. Appl. Phys. 51, 4206.
[40] Dhanaraj, G., Byrappa, K., Vishwanath, V., 2010. Handbook of Crystal Growth, Springer, Verlag Berlin Heidelberg.
[41] Föll, H., n/d. Defects in crystals (availabe online in http://www.tf.uni-kiel.de/matwis/amat/def_en/overview_main.html).
[42] Voronkov, V., 1982. J. Cryst. Growth 59, 625.
[43] Voronkov, V., Falster, R., 1999. J. Appl. Phys. 86, 5975.
[44] Voronkov, V., 1982. The mechanism of swirl defects formation in silicon, Journal of Crystal Growth, 59 (1982) 625-643.
[45] Voronkov, V., Falster, R., 2011. Intrinsic point defects in silicon crystal growth, Solid State Phenomena, 178, 3-14.
[46] Voronkov, V., Falster, R.,1999. Grown-in microdefects, residual vacancies and oxygen precipitation bands in Czochralski silicon, Journal of Crystal Growth, 204, 462-474.
[47] Falster, R., Voronkov, V., Quast, F., 2000. On the properties of the intrinsic point defects in silicon: a perspective from crystal growth and wafer processing, physica status solidi (b), 222, 219-244.
[48] Dornberger, E., Ammon, W. V., Virbulis, J., Hanna, B., Sinno, T., 2001. Modeling of transient point defect dynamics in Czochralski silicon crystals, Journal of Crystal Growth, 230. 291-299.
[49] Abe, T., 2000. The formation mechanism of grown-in defects in CZ silicon crystals based on thermal gradients measured by thermocouples near growth interfaces, Materials Science and Engineering: B, 73, 16-29.
[50] Abe, T., Takahashi, T., 2001. Intrinsic point defect behavior in silicon crystals during growth from the melt: A model derived from experimental results, Journal of Crystal Growth, 334, 16.
[51] Voronkov, V., Falster, R., 1998. Vacancy-type microdefect formation in Czochralski silicon, Journal of Crystal Growth, 194, 76-88.
[52] Petroff, P., Kock, A., 1975. Characterization of swirl defects in floating-zone silicon crystals, Journal of Crystal Growth, 30, 117-124.
[53] Föll, H., Kolbesen, B., 1975. Formation and nature of swirl defects in silicon, Applied Physics A: Materials Science & Processing, 4, 319-331.
[54] Ryuta, J., Morita, E., Tanaka, T., Shimanuki, Y., 1990. Crystal-originated singularities on Si wafer surface after SC1 cleaning, Japonese Journal of Applied Physics, 29, L1947-L1949.
[55] Graf, D., Schnegg, A., Schmolke, R., Suhren, M., Gerber, H., Wagner, P., 1997. Morphology and chemical composition of polished silicon wafer surfaces, The Electrochemical Society Proceedings, 96-22, 186-194.
[56] Yamagishi, H., Fusegawa, I., Fujimaki, N., Katayama, M., 1992. Recognition of D defects in silicon single crystals by preferential etching and effect on gate oxide integrity, Semiconductor Science and Technology, 7, A135-A140.
[57] Kato, M., Yoshida, T., Ikeda, Y., Kitagawara, Y.,1996. Transmission electron microscope observation of “IR scattering defects” in as-grown Czochralski si crystals, Japanese Journal of Applied Physics, 35, 5597-5601.
[58] Moriya, K., 1989. Observation of micro-defects in as-grown and heat treated Si crystals by infrared laser scattering tomography, Journal of Crystal Growth, 94, 182-196.
[59] Wijaranakula, W., 1994. Characterization of crystal originated defects in Czochralski silicon using nonagitated Secco etching, Journal of the Electrochemical Society, 141, 3273-3277.
[60] Zhang, J., Liu, C., Zhou, Q., Wang, J., Hao, Q., Zhang, H., Li, Y., 2004. Evolution of flow pattern defects in boron-doped <100> Czochralski silicon crystals during secco etching procedure, Journal of Crystal Growth 269, 310-316.
[61] Brown, R. A., Wang, Z., Mori, T., 2001. Engineering analysis of microdefect formation during silicon crystal growth, J. Cryst. Growth 225, 97-109.
[62] Hasebe, M., Takeoka, Y., Shinoyama, S., Naito, S., 1989. Formation process of Sracking Faults with Ringlike Distribution in CZ-Si Wafers, Jpn. J. Appl. Phys. 34, 1999-2002.

[63] Angelskåra, H., Søndenå, R., Wiig, M. S., Marstein, E. S., 2012. Characterization of oxidation-induced stacking fault rings in Cz silicon: Photoluminescence imaging and visual inspection after Wright etch, Energy Procedia 27, 160 – 166.

[64] Hu, Y., 2012. Characterization of defects in n-type CZ silicon for solar cells, PhD thesis, NTNU.

[65] Haunschild, J., Reis, I. E., Geilker, J., Rein, S., 2011. Detecting efficiency-limiting defects in Czochralski-grown silicon wafers in solar cell production using photoluminescence imaging, Phys. Status Solidi RRL 5, 199-201.

[66] Kock, A. J., Wijgert, W. M., 1980. J. Cryst. Growth 49, 718.

[67] Watkins, G. D., 1999. ECS Proc. 99-1.

[68] Voronkov, V., Falster, R., 2000. Dopant effect on point defect incorporation into growing silicon crystal, Journal of Applied Physics 87, 4126.

[69] Dornberger, E., Gräf, D., Suhren, M., Lambert, U., Wagner, P., Dupret, F., Ammon, W. V., 1997. Influence of boron concentration on the oxidation-induced stacking fault ring in Czochralski silicon crystals, Journal of Crystal Growth, 180, 347-352.

[70] Porrini, M., Voronkov, V., Falster, R., 2006. The effect of carbon and antimony on grown-in microdefects in Czochralski silicon crystals, Materials Science and Engineering: B, 134, 185-188.

[71] Kock, A., Wijgert, W. V., 1980. The effect of doping on the formation of swirl defects in dislocation-free Czochralski-grown silicon crystals, Journal of Crystal Growth, 49, 718-734.

[72] Kulkarni, M. S., Libbert, J., Keltner, S., Muléstagno, L., 2002. A theoretical and experimental analysis of macrodecoration of defects in monocrystalline silicon, Journal of the Electrochemical Society, 149, G153-G165.

[73] Yang, K., 1984. An etch for delineation of defects in silicon, Journal of the Electrochemical Society, 131, 1140-1145.

[74] Bali, M., Kentsch, J., Brendel, R., Schulz, M., 2000. Lifetime mapping of Si wafers by an infrared camera (for solar production), Proceedings of 28th IEEE Photovoltaics Specialists Conference (PVSC), 99-103.

[75] Sinton, R. A., Cuevas, A., Stuckings, M., 1996. Quasi-steady-state photoconductance, a new method for solar cell material and device characterization, Proceedings of 25th IEEE Photovoltaics Specialists Conference (PVSC), 457-460.

[76] Isenberg, J., Riepe, S., Glunz, S. W., Warta, W., 2003. Imaging method for laterally resolved measurement of minority carrier densities and lifetimes: Measurement principle and first applications, Journal of Applied Physics, 93, 4268-4275.

[77] Schofthaler, M., Brendel, R., 1995. Sensitivity and transient response of microwave reflection measurements, Journal of Applied Physics, 77, 3162-3173.

[78] Schuurmans, F. M., Schmidt, J., Sinke, W. C., Aberle, A. G., 1997. A comparative study between light-biased MW-PCD and MFCA measurements on high-quality surface passivated silicon wafers, Netherlands Energy Research Foundation ECN.

[79] Schmidt, J., 1999. Measurement of differential and actual recombination parameters on crystalline silicon wafers (solar cells), IEEE Transactions on Electron Devices, 46, 2018-2025.

[80] Stokkan, G., Sabatino, M. D., Olaisen, B. R., Søndenå, R., Dahl, Ø., 2011. Characterisation Techniques for Silicon Solar Cells Report, NTNU, SINTEF, IFE.

[81] Trupke, T., Mitchell, B., Weber, J. W., McMillan, W., Bardos, R. A., Kroeze, R., 2012. Photoluminescence Imaging for Photovoltaic Applications, Energy Procedia 15, 135 – 146.

[82] Trupke, T., Bardos, R. A., Abbott, M. D., Chen, F. W., Fisher, K., Cotter, J. E., 2006. Luminescence imaging: an ideal characterization tool for silicon, Proceedings of 16th Workshop on Crystalline Silicon Solar Cells and Modules: Materials and Processes, Denver.

[83] Trupke, T., Mitchell, B., Weber, J. W., McMillan, W., Bardos, R. A., Kroeze, R., 2012. Photoluminescence Imaging for Photovoltaic Applications, Energy Procedia 15, 135-146.

[84] McDonald, R. E., Mossoba, M. M., 1997. New Techniques and Applications in Lipid Analysis, AOCS Press.

[85] http://spie.org/Images/Graphics/Publications/TT61_Fig1.3.jpg

[86] Shimamoto, A., Yamashita, K., Inoue, H., Yang, S., Iawata, M., Ike, N., 2003. A nondestructive evaluation method: measuring the fixed strength of spot-welded joint points by surface electrical resistivity, J. Pressure Vessel Technol. 135 (2), 021501.

[87] http://www.education.com/study-help/article/physics-help-compound-microscope/

[88] Bullis, W. M., 1975. Semiconductor measurement technology, NBS Special publication 400-25, U.S. Department of Commerce, page 7.

[89] Tokuda, Y., Kobayashi, N., Usami, A., Inoue, Y., Imura, M., 1989. Thermal donor annihilation and defect production in n-type silicon by rapid thermal, Journal of Applied Physics 66, 3651.

[90] Koji, S., Seiji, S., Seishiro, F., 2007. First Principles Analysis of Formation Energy of Point Defects and Voids in Silicon Crystals during the Cooling Process of Czochralski Method, Journal of Solid Mechanics and Materials Engineering, Volume 1, Issue 9, pp. 1175-1185.

[91] ASTM F723-99, 2003. Standard practice for conversion between resistivity and dopant density for boron-doped, phosphorus-doped, and arsenic-doped silicon, Withdrawn.